RoboFly: Towards Autonomous Flight of a Multimodal Insect-Scale Robot

Yogesh Madhavrao Chukewad

A dissertation
submitted in partial fulfillment of the
requirements for the degree of

Doctor of Philosophy

University of Washington

2020

Reading Committee:

Sawyer Fuller, Chair

Santosh Devasia

Thomas Daniel

Program Authorized to Offer Degree:
Mechanical Engineering

University of Washington

Abstract

RoboFly: Towards Autonomous Flight of a Multimodal Insect-Scale Robot

Yogesh Madhavrao Chukewad

Chair of the Supervisory Committee:
Professor Sawyer Fuller
Mechanical Engineering

Insect-sized robots have numerous applications due to their small size. For example, they can go into confined spaces where humans or larger robots cannot. These applications include gas leak detections in pipelines, search and rescue in disaster response, and crop monitoring for smart agriculture. Insect-sized flapping-wing robots draw inspiration from nature's tiny machines such as flies and bees. Earlier iterations of these robots have successfully demonstrated hovering flight. However, there are some limitations to their abilities. Prior designs consist of many discrete parts that need to be manually assembled under a microscope. There are also limitations to their locomotion abilities. These robots could not control their heading while hovering, making them infeasible for many applications involving heading control and steering. Also, these robots relied on external sources for control feedback.

This dissertation proposes a re-design of insect-sized flapping-wing robots: the UW Robofly. The idea behind the re-design is a robot that compares better with its biological counterparts in terms of autonomy. Autonomy in micro-robots can be quantified in the following three terms, which can be given equal importance: 1) Mobility autonomy, 2) power autonomy, and 3) control autonomy.

In terms of mobility autonomy, the Robofly can perform multimodal locomotion, which includes ground, water surface, and aerial locomotion. The robot can also perform open-loop landing because its center of mass is closer to the ground. The robot is also easy to fabricate

since it uses a folding mechanism that decreases the number of discrete components.

Although hovering does not require a robot to control its heading, it is crucial for various applications, including image capture and video recording. A re-designed version of the UW Robofly, Robofly-Expanded, shows the ability to steer and control its heading while hovering, making it the first at this scale to control all six degrees of freedom with only two actuators.

For power autonomy, the Robofly can carry a PV cell and onboard power electronics. It became the first robot at this scale to achieve wireless liftoff as a result of the efforts in power autonomy at UW.

Lastly, control autonomy, which aims for the robot to hover without the need for motion feedback from offboard sensors such as a motion capture arena, is addressed. The robot requires at least three sensors onboard to make it hover about a point in space without drifting away. The proposed sensors are as follows– 1) a MEMS gyroscope for attitude control, 2) an IR time-of-flight range sensor for altitude control, and 3) an optical flow sensor for lateral motion control in space. While earlier research has demonstrated flights with an onboard gyroscope and IR time-of-flight sensors, this research goes a step further and include an optical flow sensor onboard. A short flight demonstrating the ability of the robot to use the optical flow sensor data for lateral motion feedback is also presented.

The work presented here overcomes significant limitations in previous work, bringing insect-sized flapping-wing robots much closer to full autonomous functionality and mobility. Future work now primarily entails further sensor integration, devising a controllable high-voltage power supply, and incorporating a power collection and storage system.

TABLE OF CONTENTS

LIST OF FIGURES

LIST OF TABLES

ACKNOWLEDGMENTS

I would like to express my gratitude to all the people who came into my life in the last four years and made this dissertation possible. First of all, I would like to thank my advisor Sawyer Fuller for choosing me as one of his first Ph.D. students and giving me the excellent opportunity to work on cutting-edge technology. His patience while advising made me a better researcher over time. His support and faith in me helped me boost my confidence in the subject area and made me a good teacher.

I would like to thank my committee members, Santosh Devasia, Tom Daniel, and Arka Majumdar. Working with professor Devasia as a teaching assistant made me a better instructor at a graduate level. Professor Tom Daniel's funding through "The Air Force Center of Excellence on Nature-Inspired Flight Technologies and Ideas (NIFTI)" ensured that my research is on-track without any financial obstacles. I would like to thank NIFTI and its leadership for the opportunity to get involved and present my research before pioneers in the field.

I am thankful to my labmates at Autonomous Insect Robotics (AIR) Lab. Insightful discussions and collaboration taught me a lot during these four years and helped me grow as a researcher.

I feel lucky to have great friends who supported me during my time at UW. Friends from Mumbai, Arizona, and Illinois kept on pouring in their constant support to keep me going at UW. Friends who came into my life while in Seattle contributed significantly both in my professional and personal life.

I like to thank my parents, Alka and Madhav, for their encouragement during my graduate studies. This achievement would not have been possible without their love.

The constant support of my siblings, Aarti and Ganesh, played a massive role in my success.

DEDICATION

to my parents

Chapter 1

INTRODUCTION

Flying machines can vary in size from a large aircraft carrying a few people to a small drone carrying a few milligrams of payload. Though all of them can fly, the complexity of the maneuverability changes significantly as the machines' size goes down. Palm-sized quad-copters can get through confined spaces because of their faster dynamics. However, if the environment gets even more cluttered, it requires even smaller robots. Since the physics of motors and propellers used in larger machines does not scale down well to micro-machines [75, 70], designs at this scale are inspired by nature's tiny-machines: bees and flies. These machines rely of a set of flapping-wings to generate thrust and perform complex maneuvers.

Micro-robots, because of their size, can be produced at a low-cost and hence deployed in larger numbers. The larger deployment number means the swarm of n robots can explore in n different dimensions. The potential applications of flying micro-robots include gas-leak detection, crop monitoring, and search and rescue.

Despite these challenges, researchers have found ways to build systems at the micro-scale, capable of hovering flight [49]. These micro-robots used piezoelectric actuators to flap their wings, inspired by flapping-wing insects [17, 23, 24, 25]. The 81-mg dual-actuator two-winged hovering robot in [49] flew using motion feedback from offboard sensors, which tracked its position and orientation. However, the actuator-wing system is fairly complex [26], and detailed research is required to control all six degrees of freedom with two actuators and two flapping-wings.

These robots are also limited by their inability to control their heading (absolute yaw angle). Past research [32, 64] has found it challenging to control the yaw while hovering with the help of only two actuators onboard. Additionally, hovering of these robots in controlled

flights relies on offboard sensors for motion feedback data [49]. This limits the ability of the robot to fly outside of a motion capture arena. Though researchers have attached various sensors to the robot [28, 34], prior robots had only one sensor at a time and could only substitute one of the attitude, altitude and lateral position data from the offboard sensors with that from the onboard one.

1.1 Challenges

This work addresses the following main issues that have been seen in the earlier work.

1.1.1 Complex fabrication

Earlier versions of insect-sized robots were difficult to fabricate because of large number of components involved [49]. The larger the number of components, the harder is the assembly which is done by hand under a microscope. This can cause misalignment and significantly change the robot's dynamic system and its characteristics. Another design from [72] got rid of all the discrete components to come up with a design, which takes inspiration from children's pop-up books. Though this method eliminated a large number of discrete components, the fabrication of the pop-up laminate was complex.

1.1.2 Difficulty in landing

The design presented in [49] has its long axis oriented vertically, making it difficult to land without tipping over. Open-loop landing is important in case of loss of power or control signals. Legs extensions [16] and switchable electrostatic adhesion [31] have successfully demonstrated landing; however, it required additional mechanism onboard which added to the weight of the robot.

1.1.3 Limited mobility autonomy

According to [63], mobility autonomy for terrestrial robots is their "ability to traverse unknown and non-smooth terrain". We extend this definition for insect sized robots as their ability to use multiple modes of locomotion, which include terrestrial, aerial, and water locomotion [18]. A 175 mg insect-sized flapping-wing robot capable of performing multimodal locomotion, including swimming and transitioning from water to air and vice versa was presented in [14]. However, this requires de-ionized water to avoid electrical shorts causing equipment damage and shock hazard. Also, the robot was not able to walk on the ground or perform any kind of ground locomotion.

1.1.4 No heading control

Insect-sized flapping-wing robots have had difficulty controlling their heading (absolute yaw angle), as it relies on subtle changes in the drive signals supplied to the two actuators to control its degrees of freedom. [32, 64] present possible difficulties in controlling heading with the current design.

1.1.5 Limited control autonomy

As mentioned above, these insect-sized aerial robots still depend on the external motion capture arena for real-time motion feedback data. This limits the ability of these robots to hover outside the arena.

1.2 Contributions and Chapter Organization

While addressing the above limitations, the contribution of this work can be listed as follows.

1. Robofly introduces a simplified fabrication process by reducing the number of components using a folding laminate, and significantly reducing the amount of hand-assembly.

2. The new design is capable of performing open-loop landing because of its re-oriented long axis and low center of gravity.

3. The design can perform multimodal locomotion, including aerial, ground, and water surface locomotion.

4. A further modified design can perform heading control while hovering, making it the first robot to do so at this scale.

5. A set of preliminary results shows that the robot can take off with an optical flow sensor that can be used for lateral motion sensing.

The rest of the dissertation is organized as follows.

Chapter 2 presents a draft of a journal paper [18], which is under review, which evolves from a published conference paper by the author [19]. It discusses previous insect-sized robots and their limitations. These limitations include complex fabrication methods, difficulty in landing, and limited mobility autonomy. The major contributions of the paper include a fabrication process, reduction in number of parts, a new design with a low center of gravity, and the ability of the robot to perform multimodal locomotion.

Chapter 3 presents a draft of a journal paper, which is under review, that discusses the limitations of earlier insect-sized robots in controlling their heading while hovering. It then demonstrates the ability of our two-winged, dual-actuator robot to control their heading while hovering. It also presents a simple analytical model that confirms that a sufficient amount of torque is generated for controlling the heading during hovering flights. This result makes Robofly the first robot to control all six degrees of freedom with only two actuators. The paper also proposes another way to further optimize the torque about the vertical axis to generate maximum yaw effect.

Chapter 4 discusses the limitations of insect-sized flying robots in flying autonomously with onboard sensors. It then proposes a set of required sensors to go onboard the robot to

be able to fly autonomously. The work also presents preliminary results on controlling the lateral motion of the robot with an onboard optical flow sensor.

Chapter 5 presents conclusions and discussion of the work.

Chapter 2

ROBOFLY: AN INSECT-SIZED ROBOT WITH SIMPLIFIED FABRICATION THAT IS CAPABLE OF FLIGHT, GROUND, AND WATER SURFACE LOCOMOTION

The text of this chapter is a draft of a journal paper, which has been under review, that evolves from a published conference paper by the author [19]. Citations for the arXiv preprint [18] of the draft of the journal paper and the conference paper [19] are as follows, respectively. The chapter and [18] build on and use substantial portion from [19].

Chukewad, Y. M., James, J., Singh, A., and Fuller, S. (2020). RoboFly: An insect-sized robot with simplified fabrication that is capable of flight, ground, and water surface locomotion. arXiv preprint arXiv:2001.02320.

Chukewad, Y. M., Singh, A. T., James, J. M., and Fuller, S. B. (2018, October). A new robot fly design that is easier to fabricate and capable of flight and ground locomotion. In 2018 IEEE/RSJ International Conference on Intelligent Robots and Systems (IROS) (pp. 4875-4882). IEEE.

2.1 Abstract

Aerial robots the size of a honeybee (∼100 mg) have advantages over larger robots because of their small size, low mass and low materials cost. Previous iterations have demonstrated controlled flight but were difficult to fabricate because they consisted of many separate parts assembled together. They also were unable to perform locomotion modes besides flight. This paper presents a new design of a 74 mg flapping-wing robot that dramatically reduces the number of parts and simplifies fabrication. It also has a lower center of mass, which

allows the robot to additionally land without the need for long legs, even in case of unstable flight. Furthermore, we show that the new design allows for wing-driven ground and air-water interfacial locomotion, improving the versatility of the robot. Forward thrust is generated by increasing the speed of downstroke relative to the upstroke of the flapping wings. This also allows for steering. The ability to land and subsequently move along the ground allows the robot to negotiate extremely confined spaces, underneath obstacles, and to precise locations. We describe the new design in detail and present results demonstrating these capabilities, as well as hovering flight and controlled landing.

2.2 Introduction

Robots the size of common insects like a honeybee (∼100 mg) have the potential for improved performance relative to larger robots in tasks that benefit from the small size or large deployment numbers. Examples include gas leak detection, assisted agriculture, or an operation around humans without impact hazard. Historically, a key challenge for robots that small was finding a suitable manufacturing method to create the necessary sub-millimeter articulated structure and actuation systems. Additionally, actuators that are in common use in larger-scale robots, such as the electric motors that actuate the propellers in most quad-rotor style drones, do not scale down favorably to insect scale in terms of efficiency or power density [75]. This is because surface area-dependent losses such as Coulomb friction and electrical resistance take on greater importance as scale reduces [70]. Recently, however, a suitable manufacturing process and actuation technology were demonstrated that allowed for controlled flights in an 81 mg robot [49]. This robot was built using a diode-pumped solid-state laser and pin-aligned sheet adhesion to fabricate the necessary components [72], and was actuated by piezo-driven flapping wings that emulated the motion of insects [17, 23, 24, 25]. The mechanism required to convert the actuator motion to wing motion for generating aerodynamic lift is discussed in [45], in which transverse bending of wings as observed in insect flapping is investigated for efficient flapping.

This paper addresses three deficiencies of the basic design introduced in [49], introducing

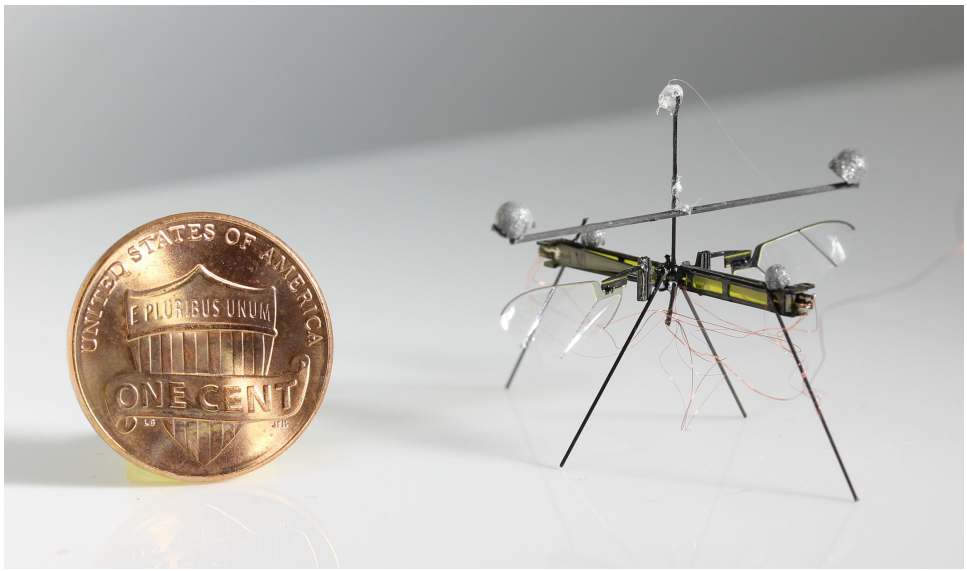

Figure 2.1: The redesigned system: University of Washington RoboFly. Each wing measures 13 mm in length and is driven by a separate piezoelectric cantilever actuator. By extending the actuators forward and aft, the center of mass is positioned near the base of the wing pair so that there is no net torque during flight. The entire robot weighs 74 mg (without retro-reflective markers). A US penny is shown for scale.

a new design that makes robot flies both more versatile and easier to fabricate.

Complex fabrication

The insect robot design of [49] suffers from being very difficult to fabricate because it requires hand assembly of a relatively large number of discrete components. It also consists of several failure-prone steps. An alternative was proposed in [72] that reduced the number of parts by taking inspiration from children's pop-up books. A robotic fly design was demonstrated that consisted of a fabrication step that required actuating a mechanism with only a single degree of freedom. But this design approach is complex, requiring 22 layers with many interdependencies between layers.

Difficulty in landing

The work in [49] demonstrating controlled flight by an 81 mg robot relied on feedback control of its upright orientation using retro-reflective marker-based motion capture. When upright, its long axis extends vertically, raising its center of mass and making it challenging to achieve a successful landing without toppling over. Successful landings with that design required leg extensions that nearly doubled the vehicle's size [16]. An alternative is to use switchable electrostatic adhesion [31] for perching and takeoffs on vertical or overhanging surfaces, but this adds complexity including a high-voltage source, requires a small amount of additional power to remain attached, and is not required for ground-based landings.

Limited mobility autonomy

Mobility autonomy for terrestrial robots can be defined as the ability to "traverse unknown and non-smooth terrain", according to [63]. Here, we define mobility autonomy for insect scale robots as their ability to traverse locomotion with multiple modes which involve aerial, terrestrial and aquatic locomotion. There have been significant developments in small scale robotics, including a 1 g miniature water strider robot [61], a robot that can jump from the

surface of water [46], a 1.6 g underwater quadrupedal robot [13], and a 175 mg flying robot capable of making the transition from water to air [14]. Here, to avoid actuators contacting water, we focus on the locomotion on the surface of the water.

A 165 mg flapping-wings water-skating robot is demonstrated in [76]. However, this robot cannot perform aerial locomotion since it propels only in the horizontal direction. The work in [14] demonstrates an aerial-aquatic flight that relies on a sparker while performing the transition from water to air. Though this robot can move itself underwater, it requires de-ionized water to avoid short-circuit and accidentally breaking actuators. Most bodies of water are not this pure, and conduct electricity, causing sudden transient arcs and actuator breakage, requiring a perfect seal on the actuators. Multimodal locomotive capabilities have been widely studied for biological species such as water striders that rely on surface tension to support their weight. An investigation of the dynamics of water walking creatures is presented in [36, 35, 12]. Hydrodynamics of water walking arthropods with characteristic length of the order 1 cm is presented in [36] and [35]. Propulsion mechanism in water striders, as presented in [35], includes momentum transfer through capillary waves and hemispherical vortices created by the driving legs. Various means of weight support at the water surface, as well as lateral propulsion for various water-walking creatures (not limited insects scale), are discussed in [12]. Propulsion mechanisms presented in the work include– 1) surface slapping (lizards), 2) rowing and walking (most of the water insects), and 3) meniscus climbing (*Pyrrhalta nymphaeae* larvae and *Mesovelia*). A quantitative biomechanical model of insects' interfacial flight is presented in [52], along with an investigation of water-lily beetles' interfacial flights. It was shown that the interfacial flight is energetically expensive as compared to aerial flights. While above-mentioned research focused on aquatic locomotion of biological creatures, the review by Kwak and Bae in [47] connects the biology with robotics by identifying robotic research in aquatic locomotion that can draw inspiration from its biological counterparts.

In light of the above limitations in fabrication, landing and mobility autonomy in previous designs, this paper describes a new design of an insect-sized flying robot, which we call the

University of Washington RoboFly (Fig. 2.1), that is intended to overcome the deficiencies of previous designs described above. Current paper evolves from authors' earlier conference paper [19], which focused on the design and fabrication of the RoboFly, and its capability to perform open-loop landing and ground locomotion. The current submission represents a significant advance over the earlier paper. It, in addition to earlier results, demonstrates how the robot can be modified with a set of passive legs to perform water-air interfacial locomotion. The earlier paper had demonstrated a stabilized takeoff; however, the current paper takes a step further to demonstrate a controlled hovering flight and closed-loop landing.

Here we report three main contributions to the design of the robot insects, which are embodied in a new design we call RoboFly.

1. This design introduces a fabrication process in which the basic wing actuation unit to be composed of a single laminate, simplifying fabrication relative to earlier designs.

2. This design has a lower center of gravity, which facilitates open-loop landing on the ground.

3. This robot also possesses better mobility autonomy with its ability to perform multi-modal locomotion which includes aerial, ground and water locomotion. The robot uses its wings to push itself along the ground and water once landed, without additional complexity and weight of a separate walking mechanism.

The rest of the paper is organized as follows. In section II, we introduce the new robot re-design and its simplified fabrication which significantly reduces the number of parts and improves the accuracy of the assembly. In section III, we discuss the ability of the robot to perform multimodal locomotion, including aerial and ground locomotion. Results from experiments from ground and aerial locomotion are also presented. In section IV, we first provide the theory behind small floating objects. We also discuss the design of hydrophobic legs which can be attached to the robot to make it float on the water surface. We also present

results from experiments from water locomotion and a transition from aerial to interfacial flight in which the robot lands on the water without breaking the surface tension film. In section V, we discuss the power consumption in the different locomotion modes.

2.3 RoboFly Fabrication

In this section we discuss the basic design of RoboFly as introduced in [19]. This robot has served as a platform for several studies, including wireless power circuit [40], a pinhole lens camera [9] on-board. Four half-flies are assembled in the work by [27]. In the current study, we focus on its design and consequent expanded locomotion capabilities.

RoboFly consists two identical subunits, each of which consists of a piezoelectric actuator, a carbon fiber airframe, and a wing. A set of four vertical legs are attached for landing and ground locomotion. The process of fabrication and assembly is explained in detail below.

Our design simplifies fabrication by combining the airframe, transmission, and actuator attachment hardware into a single laminate sheet. In the previous design that performed controlled flight [49], these consisted many separate parts. Combining these into a single laminate reduces the number of discrete parts and facilitates fabrication during prototyping. Many design features and alignment steps can be built into the design of the laminate. For example, the laminate consists of castellated folds [62] that impose a precise rotation axis, and mechanical interlocks that can constrain folds to a specific angle.

The laminate is machined and assembled using the following steps:

1. Two carbon fiber composite sheets (0°-90°-0°sheets of 27 μm thick cured prepeg) are laser machined using a diode-pumped solid-state frequency tripled Nd:Yag laser with 355 nm wavelength (PhotoMachining, Inc., Pelham, NH USA). These two sheets constitute the rigid structural material at the top and bottom of the composite layup.

2. A modified acrylic adhesive (FR1500 Pyralux, DuPont, Inc., Midland, MI) is laser machined with the same pattern as the respective carbon fiber layer features.

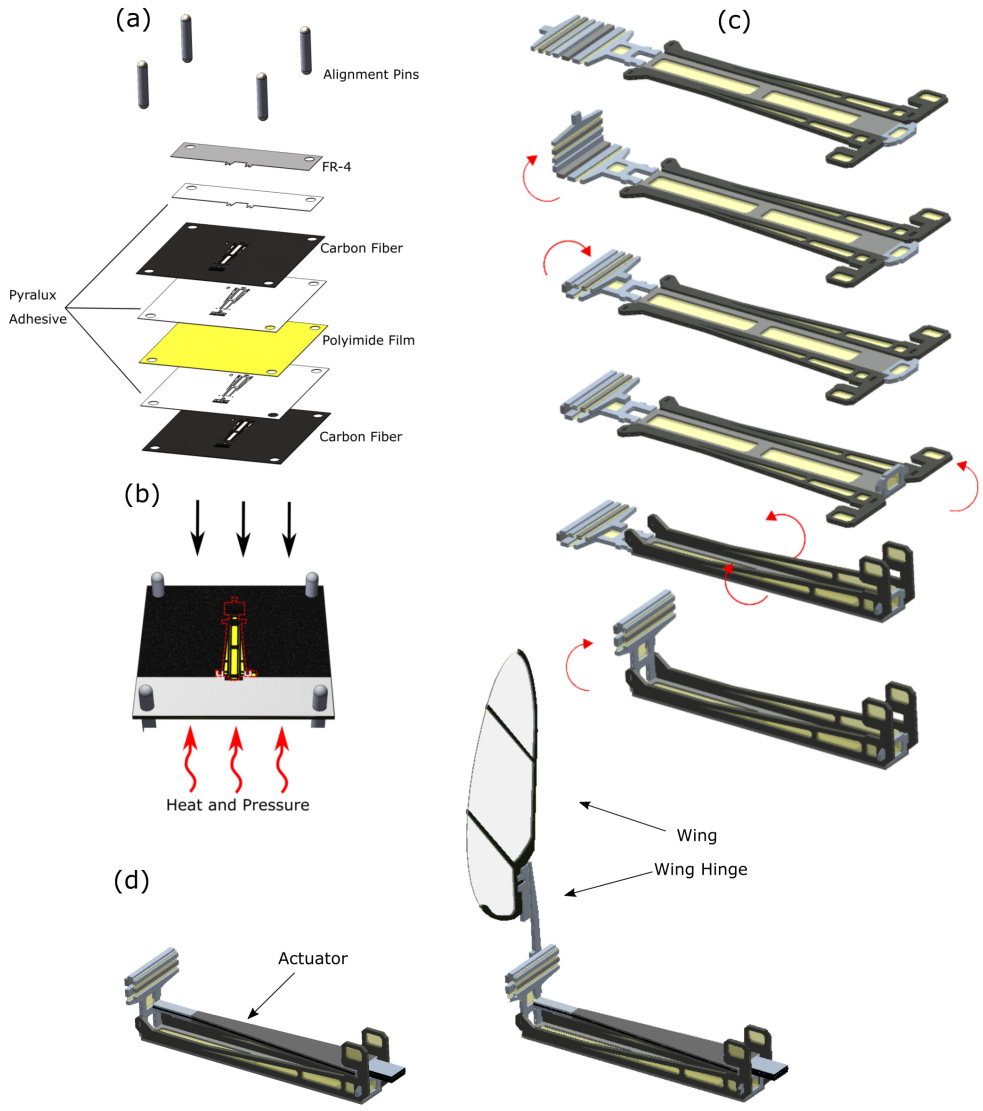

Figure 2.2: (a) An exploded view of the layup before curing. [19] © 2018 IEEE. (b) Layup during the curing process under predetermined pressure and temperature. Release cut to be done on the cured laminate is shown in red dotted lines. [19] © 2018 IEEE. (c) The released laminate is shown at the top, followed by the process involving folding of transmission and the airframe. (d) (Left) An actuator is slid into its designated slot on the airframe, (right) wing with its hinge is attached on the transmission.

3. A layer of 12.5 μm polyimide film (Kapton) is laser cut and is placed between the two adhesive layers. The thickness of the Kapton film is chosen according to the flexure feature dimension of the transmission.

4. Polished stainless steel pins align these layers, ensuring that the features are placed correctly, as shown in Fig. 2.2 (a).

5. The layup is cured in a heat press at 200°C, 480 kPa (Fig. 2.2 (b)).

6. The layup is placed back in the laser system where it is re-aligned rotationally and in translation relative to the beam. Release cuts are machined as necessary. The release cut is shown with red dotted lines in Fig. 2.2 (b).

7. Each airframe-transmission part is folded by hand with tweezers under a microscope and bonded with cyano-acrylate adhesive (Fig. 2.2 (c)).

8. An actuator is then carefully placed and bonded to the slots provided on the airframe with extra material to insure a rigid connection at its base (Fig. 2.2 (d)).

9. A wing is bonded to a wing hinge, and the assembly is then bonded to the transmission (Fig. 2.2 (d) (right)). As in [74], the wing hinge allows the angle of attack to change passively [50].

10. Two half-fly assemblies are bonded together at the middle on a specially-designed mating surface.

11. 30 μm diameter carbon fiber rods are glued to the static surface of the transmission and at the front and back extremes of the body to form the legs.

12. A wire bundle consisting of four 51-gauge insulated copper wire is then carefully soldered onto the actuators' bases to complete the electronic connections.

2.4 Multimodal Locomotion

This section discusses experimental apparatus and results. First, we describe the operation of the robot and the hardware involved in the experiments, followed by experimental results of the robot performing different types of multimodal locomotion.

2.4.1 Operation

The RoboFly has a set of four passive legs in vertical plane as shown in Fig. 2.1. This wide stance provides fabrication simplicity and facilitates landing.

The piezo actuators were driven by a desktop computer equipped with a digital-to-analog conversion board (NI 6259) running Simulink Real-Time (MathWorks, Natick, MA, USA) and amplified using three high voltage amplifiers (Trek 2205, Lockport, New York). One amplifier supplies the DC 'bias' signal to both actuators; the other two amplifiers each supply the separate sinusoidal drive signals to the two wings.

Ground locomotion is performed by flapping the wings at a lower frequency than is needed for takeoff. We chose the stroke amplitude for ground locomotion to be same as that for flight. Stroke amplitude is determined by the amplitude of the drive signal voltage (Figs. 2.3, 3.3).

The wing flapping frequency is varied depending on the mode of the locomotion that we want to carry out. However, it is kept constant for a particular mode which can be one of the following set of actions at any time instance– ground locomotion, water locomotion, and flight. Maneuvers while performing these actions were carried out by varying the voltages at which the actuators are driven. All actions besides flight are performed at non-resonant frequency to avoid accidental lift-off. Each actuator is driven at a voltage signal, $V(t) = V_0 + A_0 \sin(\omega t) + A_1 \sin(2\omega t)$, where V_0 is the offset voltage, A_0 the amplitude, $A_1 = \mu A_0$ the amplitude for the second harmonic term; a typical value μ ranges from -0.3 to 0.3. By adding a second harmonic at double the frequency, so that either the downstroke or upstroke is faster (Fig. 3.3), the robot is driven forward or backward as result of aerodynamic drag

on the wings. For example, forward motion occurs when the signal to the wings drives them rapidly backwards. A similar mechanism was proposed to induce torques about a vertical or yaw axis in [49] and [64].

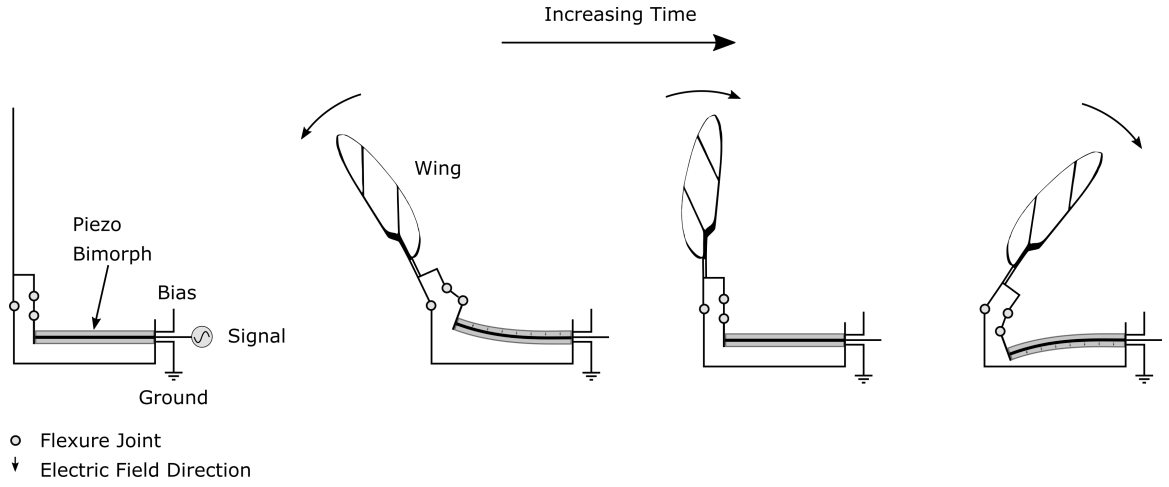

Figure 2.3: Diagram of the mechanism of piezoelectric cantilever actuation of the wings the design presented in this work. The piezo actuator drives large-amplitude wing motion through small strain changes. The piezo actuator is configured as a bimorph cantilever, consisting of a carbon fiber layer sandwiched between top and bottom piezo sheets. The top surface of the bimorph is charged to a constant high voltage, while the bottom surface is tied to ground per "simultaneous drive" configuration. An alternating signal is connected to the middle layer, providing an alternating electric field in the piezo material. This produces alternating small strains through the reverse piezoelectric effect, which is manifested as motion at the tip of the cantilever. A microfabricated transmission amplifies these tip motions into large ($\sim$ 90 deg) wing motions. This diagram shows the mechanism as seen from above; motion of the wings causes airflow downward, into the page

In case of aerial locomotion, the wings are flapped at resonant frequency to generate maximum lift. One way to determine the resonant frequency that maximizes the lift for flapping-wing micro aerial vehicles (FWMAV) is presented in [26], in which the authors

performed the system identification of an FWMAV to fit a linearized second order model.

We hypothesized that forward motion on the ground is due to the robot momentarily exceeding coulomb friction during the fast period of the wing stroke. To determine whether this motion was primarily driven by inertial or by aerodynamic forces, we performed an experiment in which the wings were replaced by carbon rods with identical mass and moment of inertia. When supplied with driving signals that moved the robot when it was equipped with wings, it was observed that the robot with carbon rods did not move significantly from its initial position. This indicates that the forces causing the ground locomotion are mainly due to the aerodynamic drag acting on the wings. To understand why this should be so, we note that the Reynolds' number of the wing is approximately 3000 [74], that is, dominated by inertial forces. This indicates that drag is proportional to the square of the wing velocity according to $f_d = \frac{1}{2} C_D \rho A v^2$, where C_D is the aerodynamic drag coefficient, ρ is the air density, A is the frontal area of the wing, and v is the velocity of the wing. Therefore, a faster wingstroke with a higher v will produce higher drag than a slow stroke.

2.4.2 Ground Locomotion

Fig. 2.5 and the supplementary video [2] show the robot performing ground locomotion along a straight line. In these trials, the wings were flapped at 60 Hz with an amplitude 210 V. Fig. 2.8 and the video [2] show that ground ambulation allows the robot to navigate under a closed door.

To determine how the driving signal affects locomotion, the RoboFly was driven in the forward direction with a range of different voltages and frequencies. Displacements were measured with a ruler, and the speed was calculated by dividing by the time taken. The results show that robot velocity increases with increasing flapping frequency and amplitude (Fig. 2.6). We conjecture that the large velocity increases that occur at different amplitudes are the result of the robot overcoming coulomb friction at a critical phase of wing flapping. The small increase from 225 V to 250 V is likely attributable to the small resulting additional stroke amplitude.

Steering is performed by varying the signals given to each flapping wing independently. To steer the body to the left, the left wing is flapped at a reduced drive signal amplitude relative to the right wing (Fig. 2.7). The rate of rotation is determined by the relative drive signal amplitude difference in the two wings. A sharp turn can be achieved by keeping one wing stationary while the other wing flaps. The extreme continuation of this would be rotation about a vertical axis passing through the center of the body, for which the wings are flapped 180°out of phase. A continuous range of turn angles can be achieved by modulating the difference between left and right wing drive signals.

Fig. 2.9 and the supplementary video [2] show that the robot is able to steer in addition to moving forward. Here, the wings were flapped at 70 Hz as above, but the left wing was flapped with larger drive signal amplitude (250 V) whereas the right wing was flapped at a lower value (200 V). Similarly, the robot was observed to steer in the other direction when these amplitudes were reversed. Moving backwards was also achieved using the appropriate driving signal.

2.4.3 Takeoff and Flight

Hovering at a specified location in space was performed using feedback from a motion capture (MoCap) system (four Prime 13 cameras, OptiTrak, Inc., Salem, OR) which tracks retroreflective markers attached on the robot. This MoCap system sends position and orientation information over Ethernet at 240 Hz to the host desktop computer which runs Simulink Real-Time.

RoboFly is an under-actuated system. However, it can move to any point in space by changing its attitude and tilting the thrust vector in the desired direction of motion. For altitude control the robot uses a proportional-integral-derivative (PID) controller to achieve desired height. The controller used by the robot for position control is shown in the block diagram in Fig. 2.10. The MoCap system, through the host computer, continuously sends the position and orientation data over the ethernet to the Simulink Target computer which runs the controller. When the controller is fed with the reference point $[x_d(t), y_d(t), z_d(t)]^T$, it

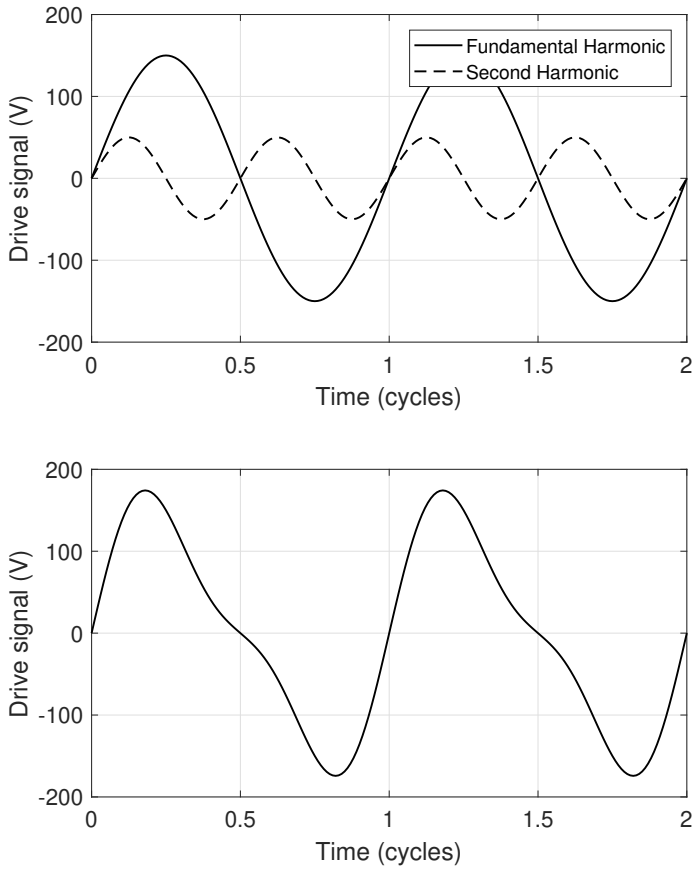

Figure 2.4: The addition of a second harmonic signal causes a differential stroke speed. (top) The sinusoidal drive signal to the wings and the second harmonic at 0.3 times the fundamental amplitude. (bottom) The sum of the two signals. [19] © 2018 IEEE.

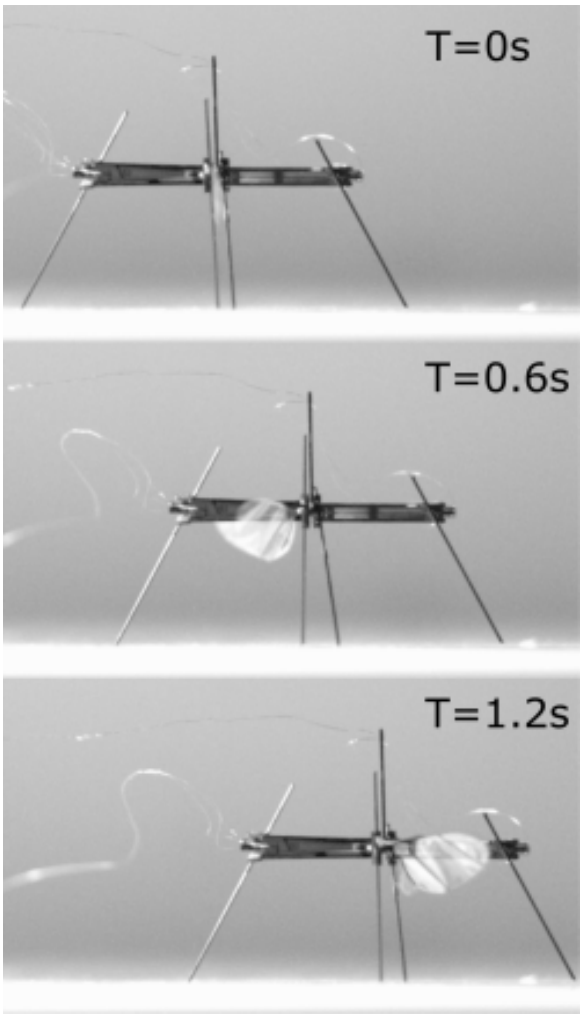

Figure 2.5: The robot moves forward over the ground when wings are flapped faster in the backward direction than the forward direction. Flapping frequency 60 Hz. In the absence of a steering command, the robot moves in a straight line

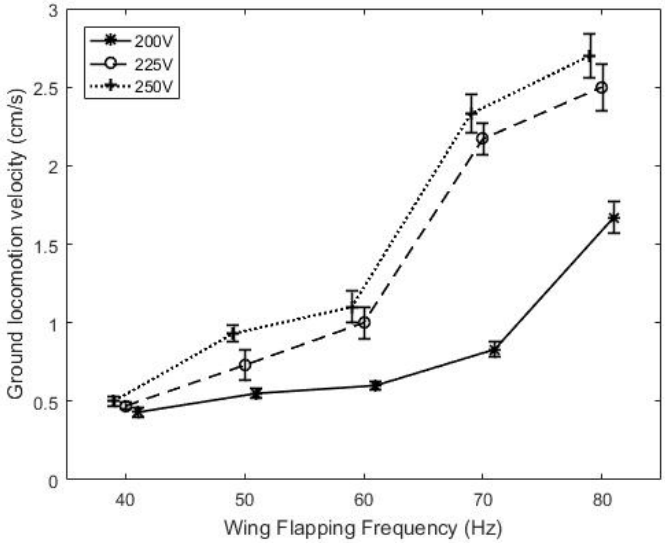

Figure 2.6: Ground locomotion velocity increases with increasing signal amplitude and flapping frequency. For comparison, liftoff occurs at approximately 140 Hz. [19] © 2018 IEEE.

varies the signal amplitude to react to the error in altitude, as mentioned above. At the same time, the controller varies the wing signal according to two control loops— inner attitude loop and outer lateral position loop, as shown in the block diagram.

As for the altitude controller which runs in parallel with the attitude controller, the height of the robot is controlled using a PID controller. The thrust generated by the wings of the robot is approximately linear with the wing amplitude. Vertical acceleration can be written by the control law as follows:

$$a_z = k_{ph} e_z + k_{dh} \dot{e}_z + k_{ih} \int_0^t e_z dt \tag{2.1}$$

where $e_z = z_d - z$ is the error between desired height z_d and current height z; k_{ph}, k_{dh} and k_{ih} are proportional, derivative and integral gains, respectively. z values received from the MoCap system are first filtered using a low-pass Butterworth filter before taking derivatives.

As for the cascaded lateral and attitude controllers, the outer loop receives the current

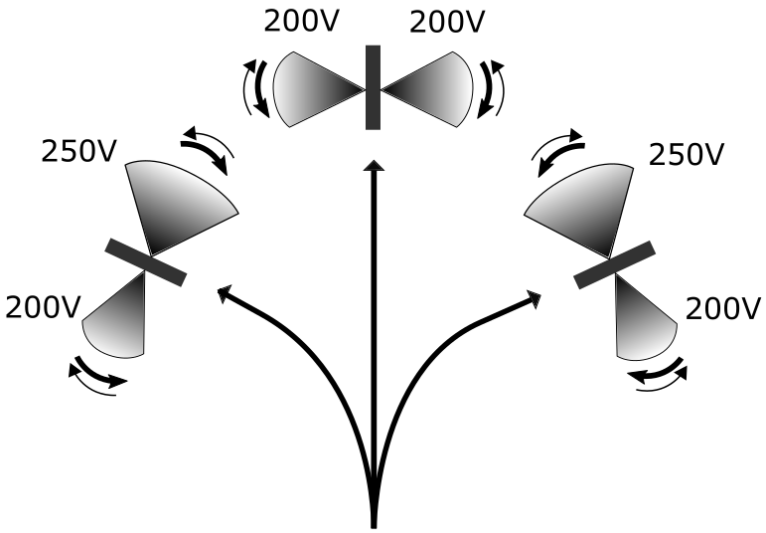

Figure 2.7: A top view of ground locomotion and steering. Steering can be performed by driving the wings with unequal signals. Thickness of the arrows corresponds to the stroke speed. Here, the rearward stroke is faster than the forward stroke, causing forward motion. [19] © 2018 IEEE.

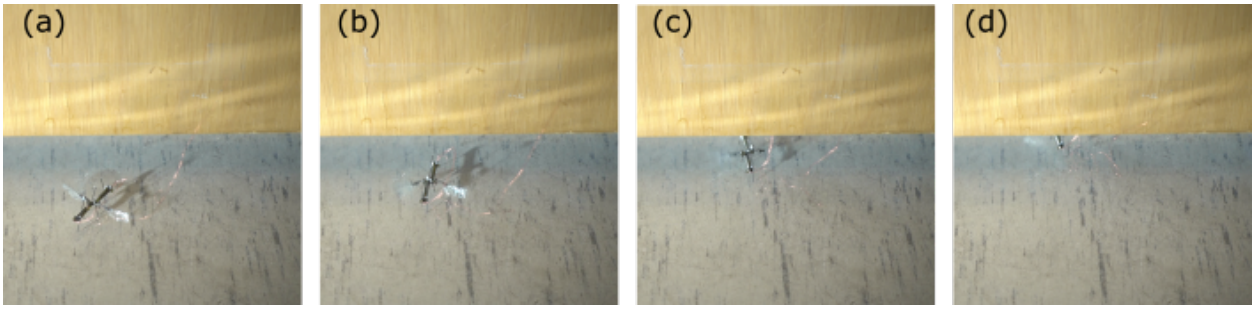

Figure 2.8: Ground locomotion allows the robot to navigate under aerial obstacles. The robot is shown ambulating under a closed door, which would not be possible by flying. [19] © 2018 IEEE.

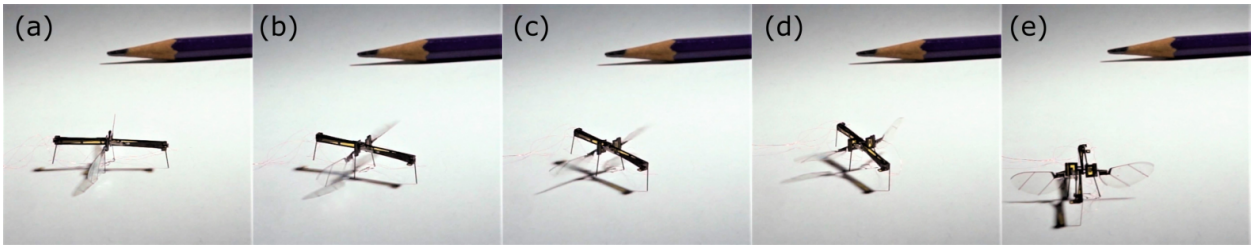

Figure 2.9: Robot turns right by 90°. A pencil tip is shown in the background for scale. [19]

and desired lateral positions in the world coordinate system. The error goes through a proportional-derivative (PD) controller, which generates a desired change in attitude vector trajectory $\hat{\mathbf{z}}_\mathbf{d}(\mathbf{t})$ which is fed into the inner attitude control loop. The outer loop assumes that the inner loop responds to attitude changes almost instantaneously.

In the outer loop, the lateral position of the robot is controlled by determining the desired inclination trajectory $\hat{\mathbf{z}}_\mathbf{d} = [\hat{z}_{dx}\ \hat{z}_{dy}]^T$. This is performed by a PD controller in the world coordinate system:

$$\hat{\mathbf{z}}_\mathbf{d} = \begin{bmatrix} \hat{z}_{dx} \\ \hat{z}_{dy} \end{bmatrix} = k_{pl} \begin{bmatrix} x_d - x \\ y_d - y \end{bmatrix} + k_{dl} \begin{bmatrix} \dot{x}_d - \dot{x} \\ \dot{y}_d - \dot{y} \end{bmatrix}, \tag{2.2}$$

where (x, y) and (x_d, y_d) are the current and desired lateral positions in global coordinate system, respectively; k_{pl} and k_{dl} are the proportional and derivative gains, respectively.

In the inner loop, attitude is controlled by rotating the robot's thrust vector towards the desired lateral position. In other words, objective of the inner loop is to align the thrust vector $\hat{\mathbf{z}} = [\hat{z}_x\ \hat{z}_y]^T$ along the desired inclination trajectory $\hat{\mathbf{z}}_\mathbf{d}$. So far we have everything in the world coordinate system; however, desired roll and pitch torques need to be determined in body-attached frame.

The robot's attitude is parameterized by a rotation matrix $\mathbf{R}$ that relates body and world coordinates according to $\boldsymbol{v} = \mathbf{R}\boldsymbol{v}'$, where we define $\boldsymbol{v}$ to be any vector expressed in world

coordinates, and $\boldsymbol{v}'$ is the same vector expressed in body-attached coordinates. The matrix $\mathbf{R}$ and body angular velocity $\boldsymbol{\omega}'$ were computed from the quaternion representation provided by the motion capture system. The error $e'_{\hat{\mathbf{z}}}$ between desired trajectory and the current thrust vector position, in body-attached frame is determined as follows:

$$\boldsymbol{e}'_{\hat{\mathbf{z}}} = \begin{bmatrix} e'_{\hat{z}x} \\ e'_{\hat{z}y} \end{bmatrix} = \mathbf{R}_2^T \left(\begin{bmatrix} \hat{z}_{dx} \\ \hat{z}_{dy} \end{bmatrix} - \begin{bmatrix} \hat{z}_x \\ \hat{z}_y \end{bmatrix} \right), \tag{2.3}$$

where $\mathbf{R}_2$ is the upper-left 2×2 block of the rotation matrix $\mathbf{R}$.

The inner faster loop for determining the roll and pitch torques in body-attached frame works as follows:

$$\begin{bmatrix} \tau_x \\ \tau_y \end{bmatrix} = k_{pa} \begin{bmatrix} -e'_{\hat{z}y} \\ e'_{\hat{z}x} \end{bmatrix} - k_{da} \begin{bmatrix} \omega'_x \\ \omega'_y \end{bmatrix} + k_{ia} \int_0^t \begin{bmatrix} -e'_{\hat{z}y} \\ e'_{\hat{z}x} \end{bmatrix} dt, \tag{2.4}$$

where k_{pa}, k_{da} and k_{ia} are the proportional, derivative and integral gains, respectively. Note that in this controller, *torque* about the x-axis depends on inclination along the y-axis and vice versa. The attitude error is the difference between desired and actual inclination. If the robot is facing in the world x-direction, the y-direction will be towards the left of the robot. In a situation where the lateral reference point in on the right of the robot, the attitude error vector will have a component in $-y$ direction. It will require the robot to perform positive roll about body x axis. This justifies the negative sign with $e'_{\hat{z}y}$ in the above expression.

The controller described above produces a thrust a_z and torques τ_x and τ_y that are normalized by body mass and moment of inertia, respectively. To map these accelerations into voltage values supplied to the piezoelectric actuators. We assume that the thrust force is linearly proportional to amplitude. To estimate the moment arm for computing torques, we approximately determined the distance between the center of mass and the aerodynamic center of thrust for individual wing, using CAD model of the robot. The yaw motion of the robot is left uncontrolled in these experiments, as it does not affect the lateral and vertical control of the robot.

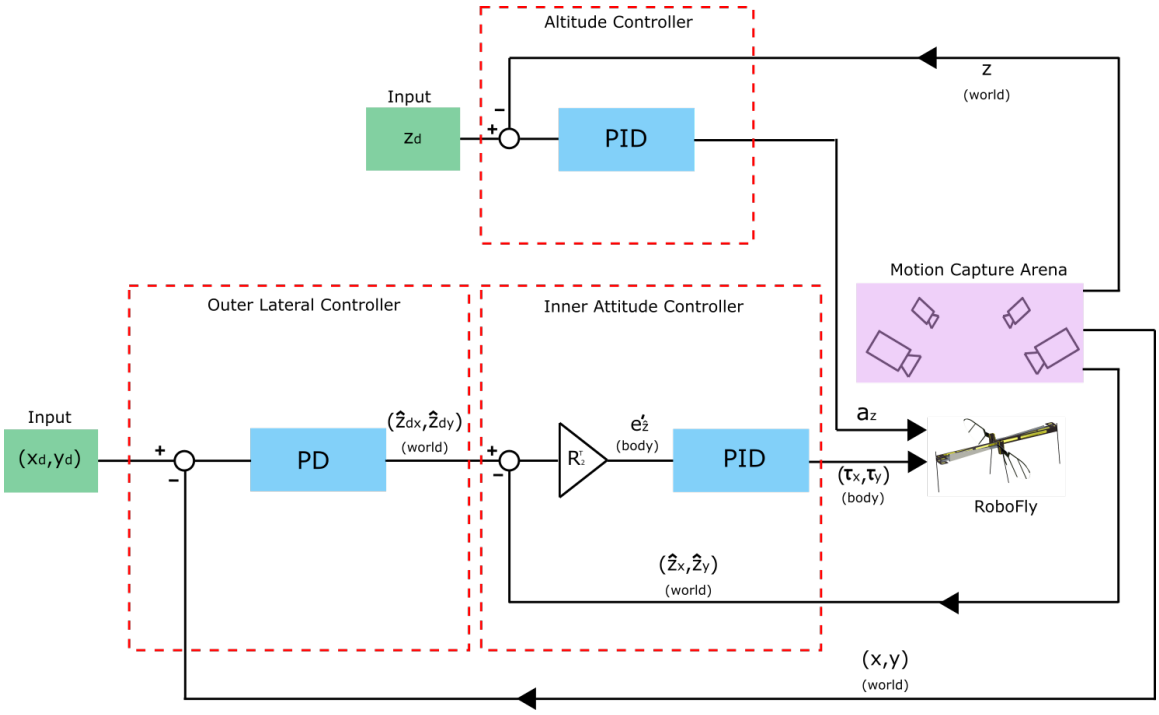

Figure 2.10: Controller used for hovering. Desired position (x_d, y_d, z_d) is fed as the input to the controller. Altitude controller, as shown at the top, achieves desired altitude z_d by generating vertical acceleration a_z. The lateral position controller works on the desired lateral coordinates to compute desired thrust vector orientation, which is fed into the inner attitude controller which determines roll and pitch torques (τ_x, τ_y). Motion capture system which tracks the position and orientation of the robot is used for the feedback.

We demonstrated controlled takeoff in Fig. 2.12. Frames from a hovering flight are shown in Fig. 2.13 where the robot was flown for around 2 seconds. The 3-dimensional trajectory plot of this flight is shown in Fig. 2.14 (a). The robot was commanded to fly at a height of 4 cm from the starting point. It can be seen in Fig. 2.14 (b) that the robot successfully maintained the height at approximately 4.5 cm from the takeoff point. The RMS position errors during the last one second of the flight were 1.8, 1.75, and 0.5 cm for its x, y, and z positions, respectively.

2.4.4 Landing

One of the objectives of the re-design reported in this work was to give the robot the capability of landing upright even in the event of loss of control, without the need of long extended-out legs as in [16]. An upright landing allows for an easy transition to the next desired task, such as walking, sensing, or subsequent flights. This is facilitated by our robot's low center of mass, which makes it harder for the robot to topple.

We demonstrated an uncontrolled takeoff as shown in Fig. 2.11. In this video, the robot is seen to be flying with unstable attitudes and landing shortly after. Under feedback control, the robot remains approximately level as shown in Fig. 2.12. Under these conditions, the robot was able to perform a landing by gradually lowering the commanded altitude as shown in Fig. 2.14 (c) which was plotted for another experiment where the robot was flown for a longer duration.

Additionally, we showed that the robot was able to land even when feedback control was not present, indicating that the lowered center of gravity of our design improves landing robustness (Fig. 2.11).

2.5 Locomotion on the Surface of Water

In this section, we show that by adding legs of the appropriate size and shape, the robot can gain an additional locomotion capability: air-water ambulation along the surface of the water.

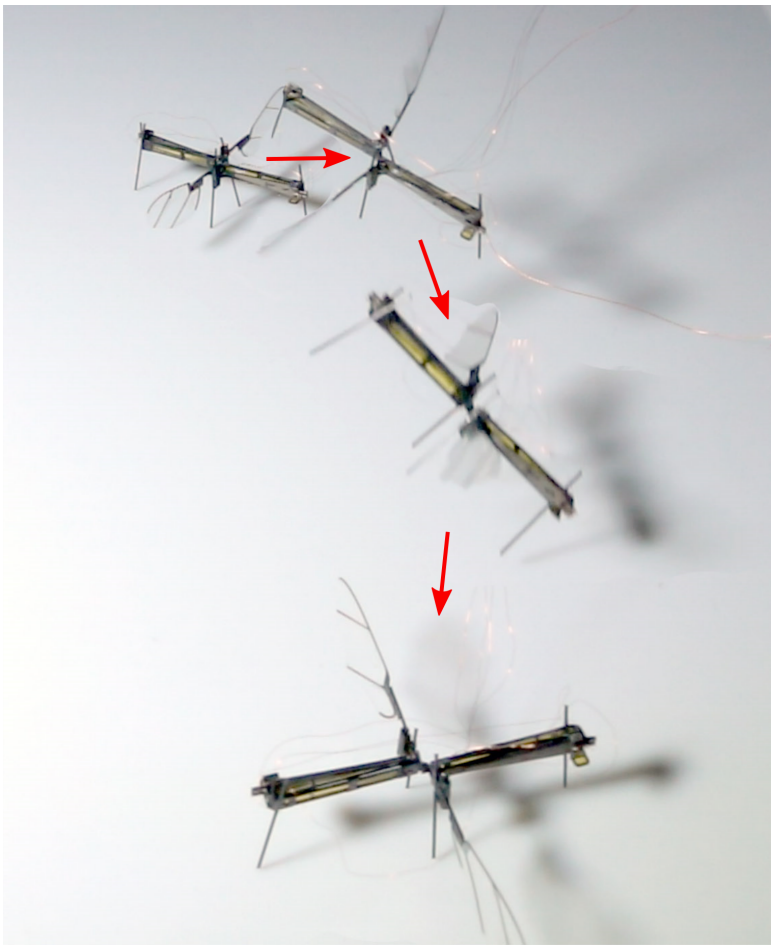

Figure 2.11: A demonstration of open-loop takeoff and landing. [19] © 2018 IEEE.

Table 2.1: Comparison of number of layers and discrete parts required in different construction methods for creating insect-sized flying robots. [19] © 2018 IEEE

	Ma [49]	Sreetharan [62]	This work
Number of Layers:	5	22	7
Number of Distinct Parts:	14	1	8

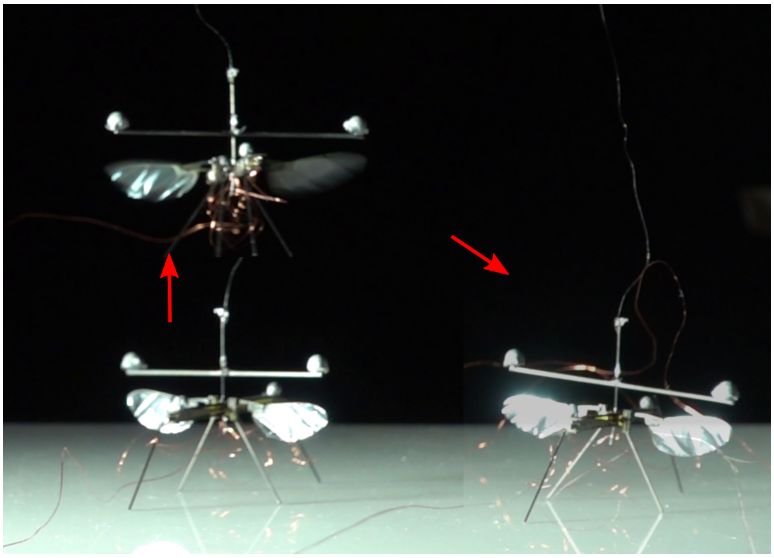

Figure 2.12: A demonstration of closed-loop takeoff and landing

2.5.1 Biological waterstriders

Our design is inspired by insects, such as stoneflies and mayflies, that use their flapping wings to push themselves along the air-water interface [52]. Like these animals, our robot moves along the surface by propelling itself with its flapping wings. Compared to an airborne RoboFly [19] which has six spatial degrees of freedom, an interfacially flying RoboFly has only three degrees of freedom because it is constrained to move along a surface. However, the surface tension forces acting on the legs of the RoboFly still makes it difficult to model the locomotion. Mukundarajan et al. [52] present a dynamic model for an interfacial flight for actual biological insects. According to this model, forces acting on an actual biological insect performing interfacial flight are as follows: 1) horizontal air drag acting on the wings, 2) horizontal capillary-gravity wave drag, 3) water drag acting on the legs at the contact with the water surface in the opposite direction to that of the motion, 4) body weight in vertical direction, 5) vertical resultant force due to surface tension, and 6) vertical water drag. The static case of the RoboFly locomotion is presented in this section.

Figure 2.13: Flight in which the robot takes off and hovers about a reference point in space with the help of feedback from a motion capture arena. The robot is subject to a small yaw bias torque that caused it to rotate leftward in this video [1].

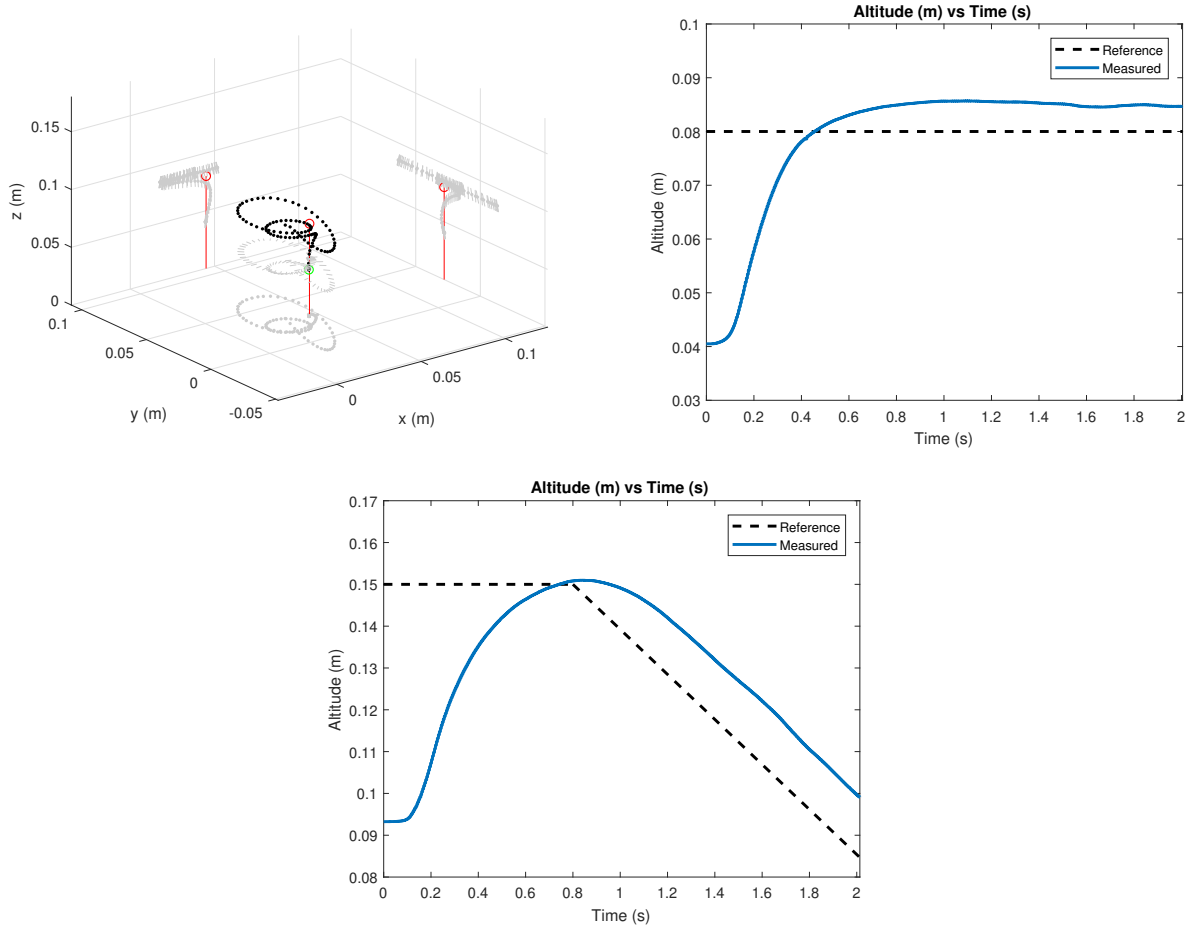

Figure 2.14: (a) Trajectory plot of RoboFly taking off and hovering about an aerial reference point. This plot corresponds to the video from which the frames in Fig. 2.13 are taken. (b) Measured and reference altitudes vs time from the hovering experiment discussed above. (c) Measured and reference altitudes vs time from the hovering experiment where the altitude is dropped linearly after some time to demonstrate the control over the altitude, which is essential for a controlled landing

In case of an object not moving or oscillating vertically, it can float on the water surface if its weight is balanced by the sum of two types of forces exerted on it. The first of these forces is buoyancy force. According to Archimedes' principle, the buoyancy force exerted on an object is equal to the weight of the water displaced. Therefore, objects with density lower than that of water tend to float, and those with density larger than that of water sink. Water-walking arthropods have density larger than water, and therefore they would sink unless supported by the second type of force which is due to the surface tension of water. This phenomenon is explained in detail in the following subsection on legs design.

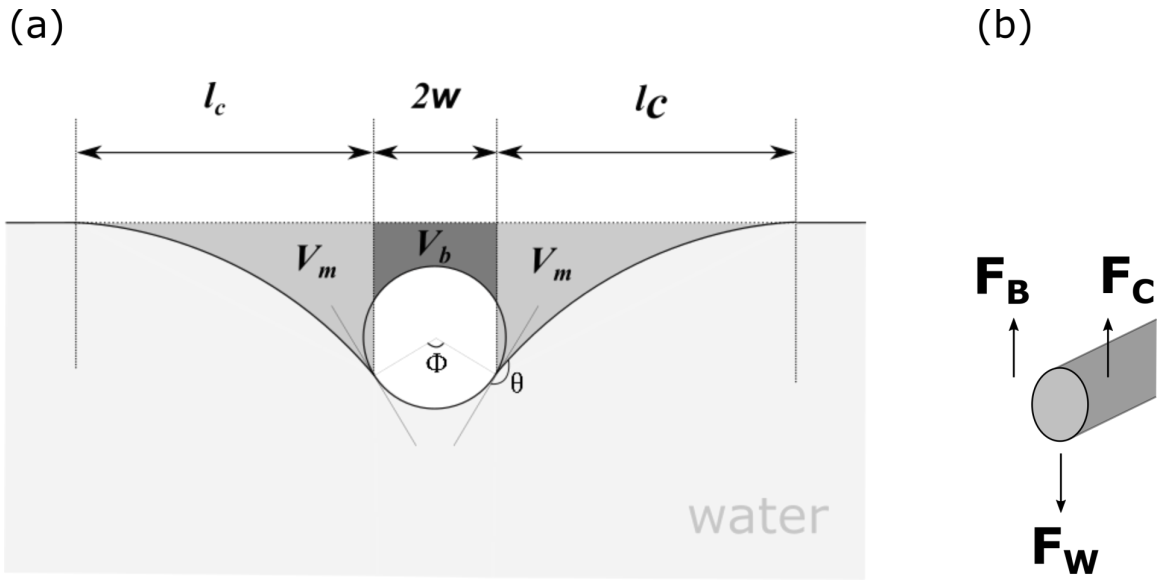

Figure 2.15: (a) Schematic showing a static state of the cross sectional view of a horizontal leg of water-walking arthropod. w is the radius of the leg, l_c is the capillary length, θ is the contact angle, ϕ is the submerged angle, V_b is the water volume displaced inside the contact line and above the body, and V_m is the water volume displaced outside the contact line. (b) Vertical loads on the supporting legs. Here, F_C is the curvature force due to surface tension, F_B the buoyancy force, and F_W the weight distribution at the point of contact.

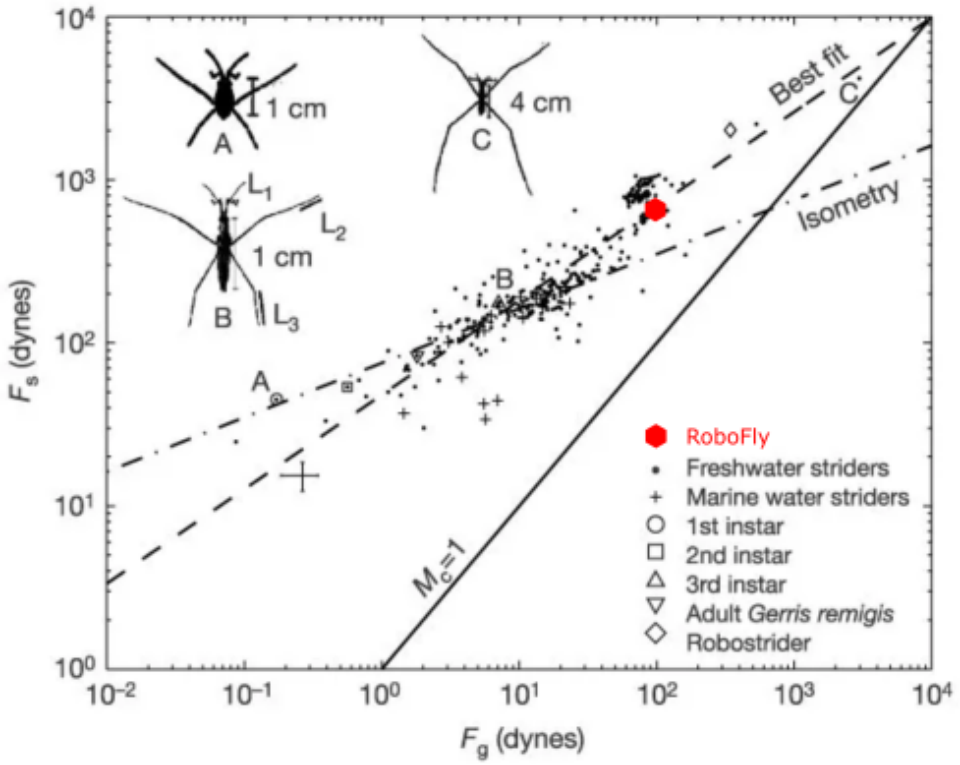

Figure 2.16: The relation between maximum curvature force and body weight for 342 species of water striders as reported in Hu, et al. [36]. Figure reproduced with "complements of John Bush, MIT" and permission from the publisher. RoboFly is shown in the red.

2.5.2 Supporting legs design using static analysis

Legs play an important role in keeping the RoboFly on the water surface without breaking the surface tension film. Rigid and compliant legs were considered in [61]. However, that study was conducted on a robot which used actuating legs for propulsion. Here, we explore the use of wings for propulsion. Therefore, to keep the design simple, a rigid and passive set of three horizontal legs are attached to the RoboFly. These legs lie in the same plane at its bottom so that every part of the legs is in contact with the ground when placed on a flat surface. Cylindrical rods are chosen over square cross-section ones for the legs to avoid complication arising due to a potential case where the robot rests or lands on an edge of a

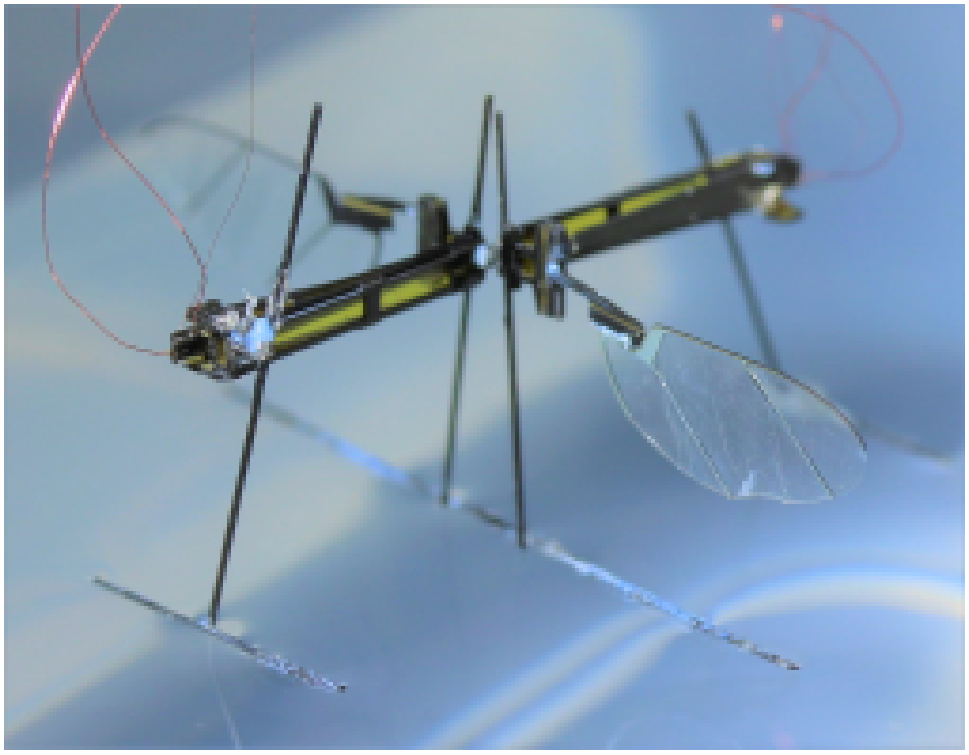

Figure 2.17: The RoboFly design weighing ∼95 mg and capable of performing multimodal locomotion including aerial, ground and air-water interfacial flights. Each wing is driven by a separate piezoelectric bimorph actuator. The surface tension force at the horizontal legs at the bottom supports the weight of the robot.

leg. A simple configuration of three parallel legs is considered for this study.

Once we know the configuration and shape of the legs, next design parameters to be considered are 1) material, 2) diameter, 3) length, and 4) distance between the rods.

The diameter of the legs plays an important role in determining the ratio of buoyancy force and curvature force. The capillary length l_c, as shown in Fig. 2.15 (a) is independent of the leg diameter and contact angle. To keep the surface unbroken it is important to have the curvature force significantly larger than the buoyancy force. A carbon fiber rod of diameter 0.5 mm was chosen for the legs. This diameter corresponds to a Bond number, $Bo \approx 0.31$,

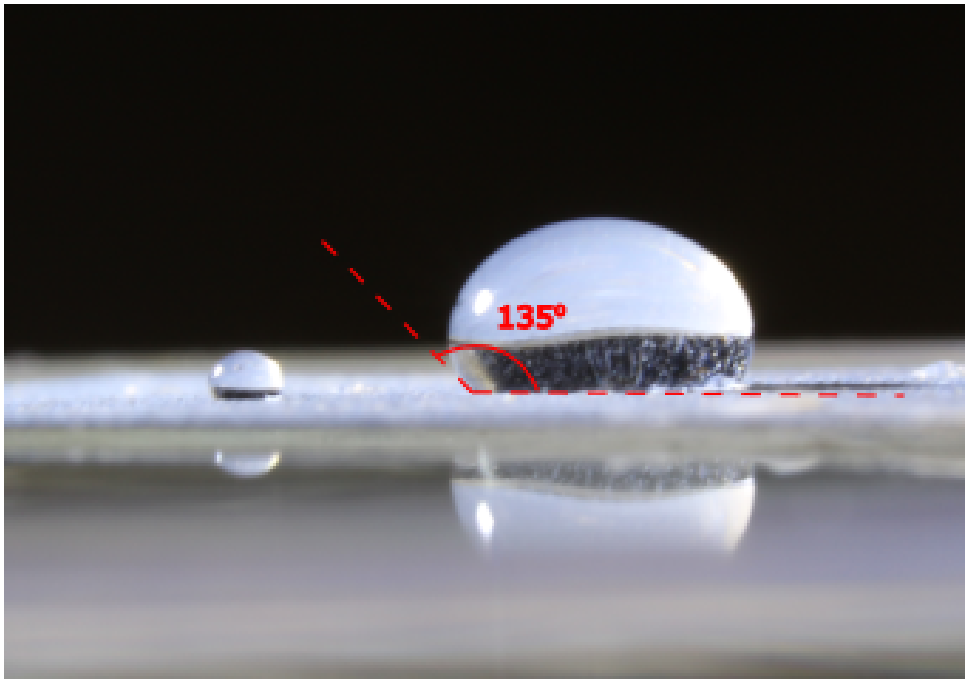

Figure 2.18: Contact angle measured and shown on a steel shim coated with hydrophobic spray *Rust-Oleum NeverWet*

as calculated later in this section. Legs made out of stainless steel were used in [61]. Here, carbon fiber rod was chosen for its strength-to-weight ratio: it weighs about 3.6 mg/cm, whereas a stainless steel rod of the same diameter weighs about 15 mg/cm. Since the goal of this robot is also to perform multimodal locomotion which includes flying, it is important to minimize mass.

While determining the length of legs, it is important to understand the forces acting on the legs while resting on the water surface. Surface tension causing curvature force is assumed to be the primary source of support to balance the weight. Buoyancy forces are not significant for the floating bodies of sub-gram weight, which is also demonstrated in [13]. Buoyancy force depends on the volume of water displaced because of the floating body, it corresponds to volume V_b as can be seen in Fig. 2.15 (a). Curvature force, on the other hand, corresponds to volume V_m displaced outside the contact line. This volume V_m depends on the capillary

length, l_c, which is determined as $l_c = (\sigma/\rho g)^{0.5} \approx 2.6$ mm for objects floating on water surfaces, where σ and ρ are coefficient of surface tension and density of water, respectively. It can be seen from Fig. 2.15 (a) that $F_B/F_c \sim V_b/V_m \sim w/l_c = 0.25/2.6 = (Bo)^{0.5} << 1$. Therefore, we can assume F_c to be a significant contributor in supporting the robot at the surface. The above expression also gives us Bo, Bond number, equal to 0.31.

For simplicity, we consider the weight F_W, as shown in Fig. 2.15 (b), to act uniformly along the entire length of all the three legs. In other words, we assume uniform weight distribution on these legs. Let's, for a moment, assume the submerged angle ϕ, as shown in Fig. 2.15 (a), is equal to 90^o. In that case, the curvature force in vertical direction F_c can be calculated as $F_c = 2\sigma L\cos(\theta)$, where L is the total length of the legs, and θ is the contact angle. From this expression, the maximum curvature force can be written as $2\sigma L$, which can be set equal to the weight to determine the minimum length of the legs, that turns out to be L_{min}=0.5 cm. However, this length of the legs is sufficient only when the entire supporting force due to surface tension acts in the vertical direction, which is not always the case. Also, the dimple due to a neighbouring leg can interfere with that of the one under study, which can reduce the supporting curvature forces as explained in [61]. Additionally, ripples that are generated due to the ground effect of flapping wings have unknown effect on the legs, and it can also reduce the supporting force at the interface. Because of these unknown effects, we turn to empirical study conducted by Hu et al. in [36]. A study of 342 species of water striders was conducted, and the relation between the maximum curvature force and body weight was found out. The plot of the relation is shown in Fig. 2.16. The best fit line of the plot of this data was given by $max(F_c) = 48F_W^{0.58}$, where the forces are measured in dynes. Considering a 80 mg robot, $max(F_c) \approx 600$ dynes, which corresponds to $L \approx 4.2$ cm. This length of legs will add an extra mass of $\sim$ 15 mg to the robot, which is compensated by further changing the total length of legs to 5 cm. So, the set of horizontal legs now consists of three pieces with the center one 2.5 cm long and other two 1.25 cm each. RoboFly is also compared with other water striders in Fig. 2.16.

Special attention is given to the minimum distance between two adjacent legs. If they

are too close, the dimple caused by a leg on the water surface will interfere with that by its neighbouring legs. This will reduce the lift force generated by the surface tension at the contact with legs, this is shown in the study by [61] about the deformed water profile reducing the lift force. For a static case, it can be seen in their work that the dimple dies down at about 6 mm from a floating object, which requires us to have at least 12 mm of gap between legs. Keeping that in mind, we choose to have them 15 mm apart to be in safe situation in dynamic case in which the robot will be performing water locomotion.

2.5.3 Experimental results

The signal generated in this case is similar to the one used for ground locomotion. When the wings are flapped, ripples can be seen generating and propagating away from the robot on the water surface. Though the effect of ripples is unknown on the motion of the robot, it is observed that the robot doesn't move in any direction when the two wings are driven by the same driving signal without any second harmonic component. It can be concluded that the ripples have equal effect in all directions, and thus can be ignored in the dynamic force balance in the horizontal plane.

RoboFly with its horizontal legs is shown in Fig. 2.17. The design parameters for the legs are summarized in Table 2.2. As mentioned in above section, RoboFly has the capability to move in either direction. Frames captured from a video of RoboFly moving from left to right are shown in Fig. 2.19. The robot in this video was driven with a second harmonic signal of amplitude 220 V, and the wings were flapped at 35 Hz, far below its resonant frequency. The recorded speed of this interfacial flight was $\approx$0.5 cm/s. In addition to the straight-line motion, the robot can also steer by flapping one wing at a larger amplitude than the other. The robot can be seen taking a sharp turn towards left in Fig. 2.20 by flapping the right wing at a larger amplitude (220 V) than the left one (180 V). The angular speed is recorded as $\approx 20^o$ per second. Fig. 2.21 shows a set of images in which an airborne robot is seen to be landing on the water surface. In this case, the robot simply jumps off the cardboard box in the background. It can be seen that the robot didn't land in its stable orientation; however,

it still manages to recover without breaking the surface tension of the water. This can be attributed to the length of the legs being inspired by the actual biological species which may not have all the legs touching the water surface all the time. However, stabilized attitude and controlled descent are essential to consistently observe water surface landing.

Table 2.2: Summary of design parameters of leg

Design Parameter	Value/Characteristic/Name
Number of legs	3
Cross-section	Cylindrical
Material	Carbon fiber
Diameter	0.5 mm
Total Length	50 mm
Distance between adjacent legs	15 mm
Hydrophobic Coating	*Rust-Oleum NeverWet*
Contact angle	135^o (Fig. 2.18)

2.5.4 Challenges

When the robot tries to take off, it relies on the wing lift to generate enough thrust to break its contact with the water surface. Immediately preceding the contact breakage, the surface tension which pulls the robot back assumes its maximum value, $2\sigma L$. If we assume, in a failed attempt of take-off, the robot comes to a static position right before the contact breaks, the meniscus assumes the maximum height. For the static analysis at this position, we can set the buoyancy force F_B equal to zero as robot legs are at their maximum height

on the water surface. This will reduce the equation of motion to as in (2.5).

$$F_L = F_W + F_{C,max} \tag{2.5}$$

Now, substituting $F_{C,max} = 2\sigma L$ and values of all the unknowns, we can see that the value of F_L corresponds to 800 mg of force, which is 10 times the weight of the robot. It is impossible for this insect scale robot to lift off with an additional load of 9 times its own weight. That means it has to rely on some external factor to break the contact with the water surface. This phenomenon can be attributed to the behavior that has been observed with its biological counterpart *nymphaeae*. These insects, as shown in [52], oscillates in the vertical direction as they generate lift only in the downstroke; therefore, the meniscus is observed to be assuming its maximum height during downstroke and maximum depth during upstroke. As *nymphaeae* are seen to be taking off after some time which varies from a fraction of seconds to a few seconds, once the oscillations assume large amplitudes and the inertia is large enough to break the surface.

In *nymphaeae* study, the required lift-to-weight ratio is observed to be $q = 3.4$, whereas it is observed to be $q \approx 10$ in the case of its robotic counterpart. The transition from iterfacial flight to airborne flight with the help of induced oscillations is considered to be out of scope for this paper.

2.5.5 Comparison with other biological locomotion

The locomotion of aquatic and semi-aquatic insects can be characterized using the thrust generating mechanism. The water surface locomotion shown by RoboFly is similar to most semiaquatic insects which utilize their hydrophobic legs for flotation and propulsion. This locomotion is known as water walking. Water walking insects also rely on surface tension for flotation as reviewed in [36, 35, 12].

Another locomotion inspired by Marangoni propulsion of rove beetle and semiaquatic insects like *Microvelia* and *Velia* is reviewed in [12]. In this locomotion, the thrust is generated by uneven surface tension because of a chemical released by the insects.

Honeybees, when trapped on the water surface, show a unique type of locomotion referred to as hydrofoiling locomotion by [57]. Honeybees are seen to be using their wings as hydrofoils to generate hydrodynamic thrust. Another interesting locomotion on water surface similar to honeybee's hydrofoiling locomotion is the rowing locomotion shown by the stonefly as reported in [51]. This locomotion makes use of both hydrodynamic drag as well as aerodynamic lift for propulsion.

Figure 2.19: Robot performing water surface locomotion with open loop control by flapping wings at 35 Hz, frames are captured at 0, 4, 8, and 12 s

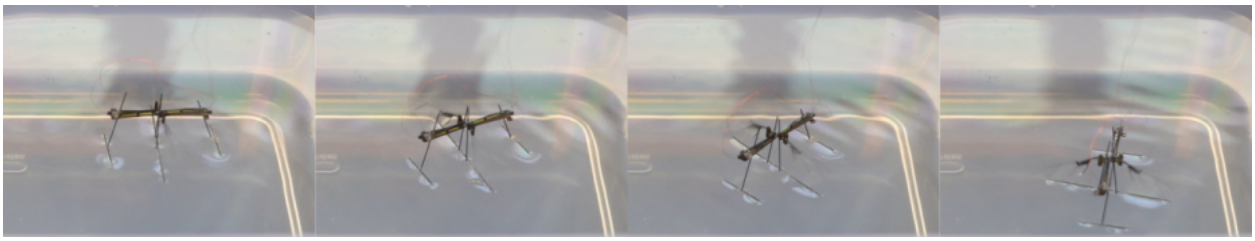

Figure 2.20: Robot performing water surface locomotion and turning left with open loop control by flapping wings at 30 Hz, frames are captured at 0, 1, 2, and 3 s

2.6 Power Consumption

The cost of transport (CoT) is a useful metric to compare different modes of locomotion. CoT is defined as the energy expense per unit distance traveled, or equivalently the power required per unit velocity, as shown in Eq. 2.6. To calculate CoT for the robot, voltage and

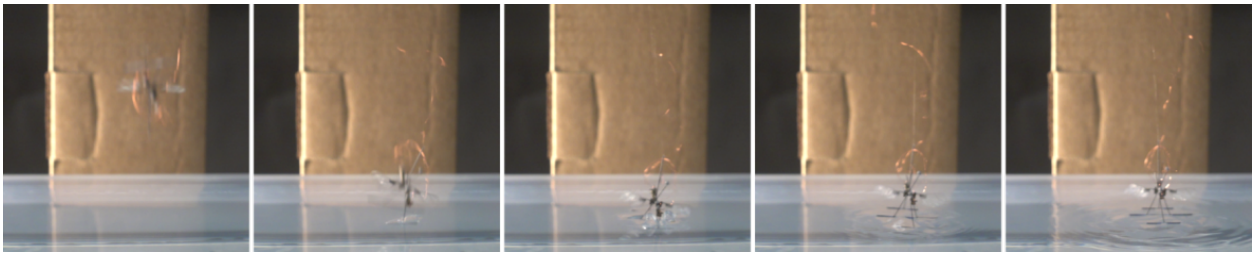

Figure 2.21: Airborne RoboFly landing on the water surface. Frames are captured at 0 ms (robot is still airborne), 30 ms (landing only on front leg), 45 ms (middle leg also gets in contact with the water surface), 95 ms (all three legs are in contact now) and 145 ms (oscillations are damped and the robot is stable).

current supplied to the bimorph actuators was measured at a sampling frequency of 10 kHz, from the voltage and current monitor outputs of the amplifiers (Trek 2205, Lockport, New York). The instantaneous power was time averaged over an integer number of wing strokes in order to compute the average power consumption of the robot.

In order to estimate power requirements for an untethered robot, we envision a linear half-bridge driver circuit such as demonstrated in [40]. In comparison to the desktop amplifiers, the onboard linear actuator driver would add inefficiency which would increase power requirements above what we measure for the tethered robot powered by the desktop amplifiers. Therefore, to estimate the power requirements an untethered robot, reverse power from the center node of the parallel-connected bimorph actuator is zeroed when computing the integral of V, I_r in Eq. 2.6. This assumption reflects the reality for linear half-bridge piezo driver methods that during the part of the wing stroke in which the sinusoidal drive signal voltage is decreasing, positive charge leaving the center node of the actuator must be dumped to ground through the transistor elements of the driver, and that energy cannot be recovered to the high voltage bias rail or back to the boost converter power source. Alternate driver topologies which are capable of bidirectional power flow [39] or which implement the energy recovery discussed in [43], can be somewhat more efficient than this proposed linear

driver, so the power consumption and CoT computed here provides an upper bound of power requirements. The integral of the measured voltage V and current I from the amplifiers represents the lower bound of predicted power autonomous robot requirements because that would assume perfect driver efficiency.

Eq. 2.6 shows the computation of the cost of transport (CoT), that is, the energy used per unit distance traveled. The measured power was integrated over time and divided by the estimated distance traveled by the robot as measured by the motion capture system.

$$CoT = \frac{\int V I_r \, \mathrm{d}t}{S} \tag{2.6}$$

Where S is the 3D distance traveled, V is the driving voltage, and I_r is the measured current.

To measure CoT for ground ambulation, we set the driving amplitude to 250 V. The results show that the cost of transport decreases with increasing flapping frequency (Fig. 2.22). This is conjectured to be the result of two competing factors: 1) Electrical input power increases proportionally with driving frequency f because the actuators are principally a capacitive load with current $I \propto C\frac{\mathrm{d}V}{\mathrm{d}t}$; 2) The aerodynamic lift increases with f^2 for the same reason that drag does (Section III). Therefore, for small frequency increases the robot is expected to reduce contact friction during ambulatory and water-striding motion faster than the power requirements increase. Together these factors suggest an inverse proportionality between CoT and flapping frequency which is observed in Fig. 2.22.

Measurements also indicated the trend of decreasing COT with increasing frequency while the robot was in flight. The COT was measured in flights traversing 0.2 m as measured by motion capture while flapping at 140 Hz. The COT for flying locomotion was ~ 0.02 mJ/mm, which is $\approx 25\times$ less than the most efficient ambulation. CoT is not an applicable metric for hovering flight at a single position. The robot consumed approximately 50 mW measured power during hovering flight with feedback controlled attitude and position.

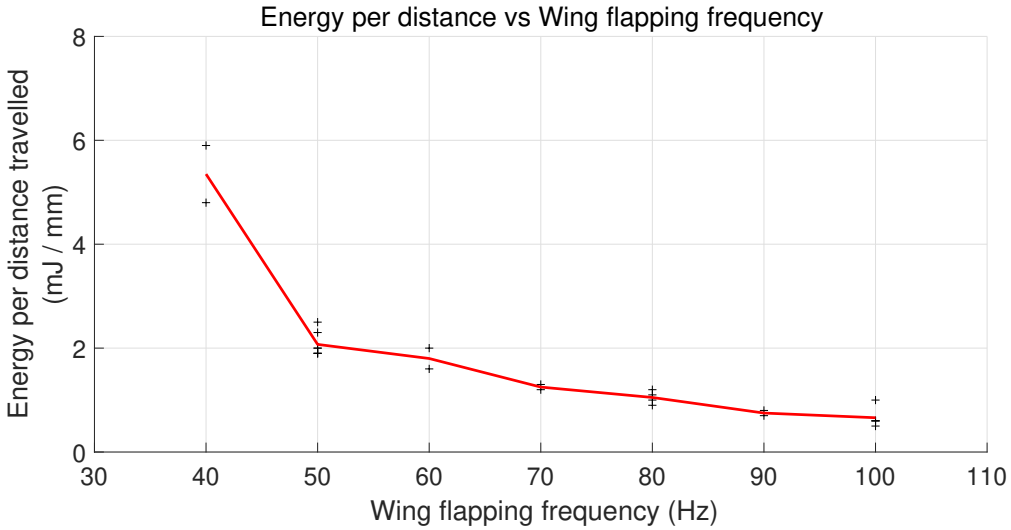

Figure 2.22: The cost of transport (COT), the energy expended per unit distance traveled, decreases with increasing drive frequency f. [19] © 2018 IEEE.

2.7 Future Work

Water locomotion can be further improved by performing a transition from water surface to airborne flight. We found that the vehicle was unable to lift off from the surface if the water simply by flapping its wings, as predicted by our earlier analysis indicating that the robot needs to lift approximately 9 times its own weight to break the water surface tension. In addition to explosive ejection [14], other potential means include: 1) electrowetting of the legs to reduce the contact angle and therefore reduce the force [13], 2) creating waves on water surface with the help of flapping wings to lower the force required to break water surface film, 3) making the robot collide with an obstacle on the water surface which could provide the necessary impulse force.

As to ground locomotion, alternative modes such as jumping are possible. Hopping locomotion can be efficient due to advantageous scaling effects as robot size and weight are reduced [7], although additional weight and complicated hopping mechanisms are ill suited

to honeybee-sized flying robots as discussed in Section III. Fei et al. [48] demonstrate bio-inspired jumping mechanisms and discusses the dynamics and optimization. Bhushan and Tomlin in [10] demonstrate an insect-sized microrobot capable of jumping 6 times per minute.

This work uses a 2-component Fourier basis to cause differential stroke speed, but we have not explored other waveforms e.g. 'sawtooth', which could perform better.

Although inertial dynamics of the flapping motion were experimentally determined to be less significant than the aerodynamic drag acting on the wings (Section II), there is still uncertainty as to the role of vibratory mechanisms in the ground locomotion. If vibratory mechanism is significant, then the feet could be redesigned to exploit this; e.g. directional spines could serve to selectively favor a direction of motion.

2.8 Conclusion

This paper presents a new design with three major contributions to the field of insect-sized robotics. It 1) simplifies fabrication, 2) allows the robot to perform landing and ground locomotion, 3) designs legs for the robot to perform water surface locomotion similar to its biological counterparts.

In the new design, the airframe and transmission are all folded from a single laminate sheet. Compared to previous work, the design presented here represents an intermediate solution that lies between the many parts of [49, 50] and the single laminate sheet composed of many layers of [62] (Table 2.1). We believe this represents a valuable intermediate between these two extremes because on the one hand our design with two laminates gains many of the benefits of pop-up book manufacturing, such as having few parts and the ability to precision align small components. And on the other hand, it does not inherit the substantial complexity imposed by large number of interdependencies among layers. This reduces the difficulty of design iteration. Furthermore, we believe our intermediate approach is still amenable to automated manufacturing, by assuming that some steps will be performed by small robotic end-effectors.

We showed that the lowered center of gravity of the robot allows it to land and ambulate

along the ground including steering, in addition to flight. It was able to land consistently under feedback control and it was even able to land upright from an unstable open-loop flight. The cost of transport was found to be substantially higher than that of free-flight, so this mode of locomotion is better suited to precise motions, such as to precisely position a sensor. We additionally showed that ground ambulation can allow our robot to reach new places that are not accessible through flight, such as moving under a typical door. This represents a capability to negotiate an obstacle that heretofore exclusively the domain of the most adept ground robots, and impossible with air robots.

We also demonstrated another locomotive capability of the robot where it can, with the help of a set of three small horizontal legs, land on water surface and perform a waterlily beetle-like locomotion along the surface.

Our robot's multimodal locomotion capabilities resemble those of larger robots. For example, [20] developed a larger bio-inspired robot (393 g, 72 cm) capable gliding flight as well as the ability to ambulate by rotating its ailerons. [8] developed a bio-inspired micro-vehicle (100 g, 30.5 cm) capable of performing aerial locomotion using wings and terrestrial locomotion using whegs. Similarly, [55] developed a bipedal ornithopter (11.4 g, 28 cm) with flapping wings for aerial locomotion and rotary legs for terrestrial locomotion. A 30 g robot took an approach similar to our robot by using the four propellers of its flight apparatus to steer its motion. These were used to steer a simple walking mechanism that was capable of moving in only one direction [53]. To our knowledge this work represents the first example of multimodal locomotion capability at insect scale.

The capability of landing will allow the robot to perform intermittent flights. This will be useful for providing power to the robot. For example, the robot could more easily collect power from a laser because the laser would not have to follow it [40, 37, 54], or from magnetic resonance coupling, as has previously been demonstrated on a ground robot in [42]. Furthermore, landing will be necessary for the robot to collect energy from ambient energy sources such as indoor light or radio frequency signals such as WiFi [66] or cellular. In the case of energy harvesting from aeroelastic flutter [11], ground locomotion may be needed to

position the robot in the flow. While these sources tend to be very minute and therefore insufficient to power larger robots, they may be enough to power the UW RoboFly for a reasonable fraction of the time, if it can land and charge between flights. The horizontal design of this work facilitates the attachment of power electronics [40] and sensors such as ultralight cameras [9].

Acknowledgment

This work is partially supported by the Air Force Office of Scientific Research under grant no. FA9550-14-1-0398. The authors also wish to thank Haripriya Mukundarajan, PhD student at Prakash Lab, Stanford University for insightful discussions during the study on water surface locomotion.

Chapter 3

YAW CONTROL OF A HOVERING FLAPPING-WING AERIAL VEHICLE WITH A PASSIVE WING HINGE

The text of this chapter is a draft of a journal paper, which is under review. It discusses earlier insect-sized robots' limitations in controlling the heading while hovering. It then demonstrates the ability of our two-winged, dual-actuator robot to control the heading while hovering. It also presents a simple analytical model that confirms sufficient torque is generated to control the heading while in mid-flight. This results makes Robofly the first robot to control all six degrees-of-freedom with only two actuators. The paper also presents some preliminary work on how to further optimize the torque about the vertical axis to generate maximum yaw effect.

Chukewad, Y. and Fuller, S. (2020). Yaw control of a hovering flapping-wing aerial vehicle With a passive wing hinge, IEEE Robotics and Automation Letters (RA-L) with ICRA 2020 conference option (Under review).

3.1 Abstract

Flapping-wing insect-scale robots (<500 mg) rely on small changes in drive signals supplied to actuators to generate angular torques. Previous results on vehicles with passive wing hinges have demonstrated roll, pitch, and position control, but they have not yet been able to control their yaw (heading) angle while hovering. To actuate yaw, the speed of the downstroke can be changed relative to the upstroke by adding a second harmonic signal at double the fundamental flapping frequency. Previous work has shown that pitching dynamics of a passive spring-like wing hinge reduces the aerodynamic drag available to produce yaw torque. We introduce three innovations that increase yaw actuation torque: 1) a new two-

actuator robot fly design that increases the moment arm, 2) wider actuators that increase the operating frequency, and 3) a phase shift to the second harmonic signal. We validated these results through simulation and experiment. Further, we present the first demonstration of yaw angle control on a passive-hinge vehicle in a controlled flight. Our new robot fly design, UW Robofly-Expanded, weighs 160 mg (two toothpicks) and requires only two piezo actuators to steer itself.

3.2 Introduction

Insect-scale flying robots (<500 mg) have the potential for several applications such as search and rescue, surveillance, and environmental monitoring, due to their small size and large deployment numbers. First feedback-controlled hovering of an insect-robot, RoboBee, was demonstrated in [49], in which all but the yaw degree of freedom were controlled. Another design, Robofly, at the similar size was introduced in the authors' earlier work in [19, 18]. Robofly introduced a new design that is easier to fabricate and capable of performing multi-modal locomotion including ground and water locomotion in addition to flying.

The challenges at micro-scale include aerodynamic forces, sensing, control, and power. With recent developments in power electronics, the first wireless lift-off of a two-winged insect-scale robot was achieved in [40] and a four-winged robot in [39]. Aiming toward control autonomy, [28] included a gyroscope for attitude feedback, [29] included a ocelli-inspired vision sensor, and [33] included a magnetometer for pitch and yaw feedback. Fuller in [27] introduced a four-winged micro-scale robot for better control authority and improved payload. Another two-winged version of Robofly was introduced in [22] with the robot's long axis re-oriented along the pitch axis for better control authority. Its wider actuators also allowed for improved payload capability.

Despite recent developments in sensing, we are yet to see an insect-sized dual-actuator robot with controlled heading or yaw angle (see Fig. 3.1 for yaw axis) while hovering. As mentioned in [30], control of the yaw angle of the robot is desirable for many reasons including, 1) legs required to be in specific orientation for landing, 2) sensor (for example, camera

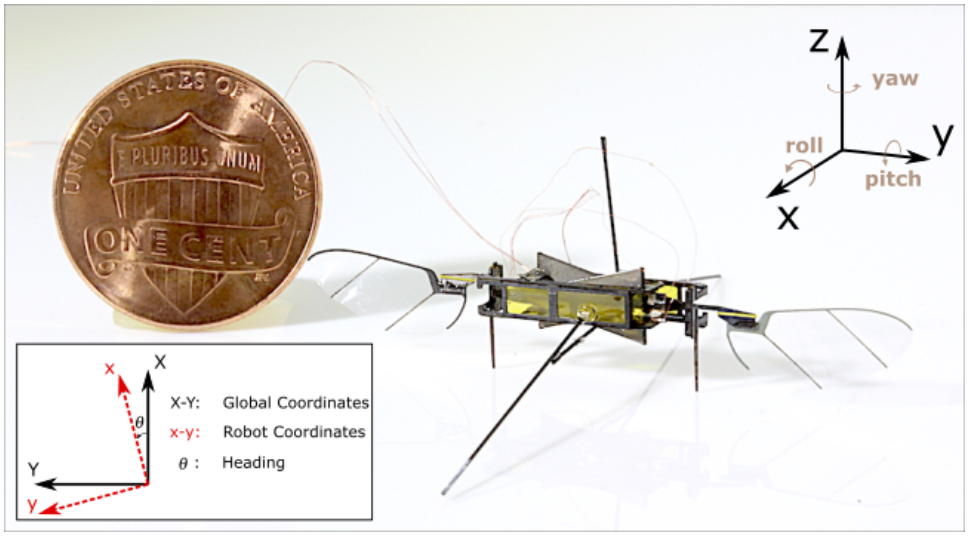

Figure 3.1: Robofly-Expanded, a new design of a robot fly [22]. A U.S. penny is shown for scale. Inset shows how heading (absolute yaw angle) θ is measured between world and robot coordinate systems, about the positive world Z-axis. © 2020 IEEE.

and IR sensor) required to point in a particular direction, or 3) to reduce computation complexity of the controller (a computationally intensive switching between global and body coordinate frames for lateral position control can be reduced or completely eliminated).

The challenge of yaw actuation in passive-hinge vehicles is not new. Flapping with a passive hinge represents a distinct class of aerodynamic system with behavior that differs from systems in which wing motion is entirely specified [65]. Yaw torque measurements in the two-actuator Harvard Robobee affixed to a capacitive torque sensor suggested the ability to produce significant yaw torque [50]. The technique relied on its piezo actuator's ability for high-bandwidth actuation, by flapping the wing in one direction faster than the other direction. Air drag varies approximately with velocity squared in the inertia-dominated fluid mechanics of this scale (Re ≈3000 [74]), so that the net stroke-averaged drag force can be varied. But in videos of its first controlled flights it can be observed that yaw angle rotated freely [49]. Indeed, significant efforts needed to be undertaken in that work to design a nonlinear controller that could operate regardless of orientation. For this reason it is likely

that the previously -measured yaw torques could be attributable to sensing error.

At insect scale, the most successful previous demonstration is hovering control of the yaw came in a design with two extra actuators [67], for a total of four. A sophisticated linkage allowed this robot to vary the wing hinge, to actuate the angle of attack (AoA) to actuate yaw [69]. Like flies, this robot used a passive wing hinge whose neutral angle was under active control [68]. Larger flapping wing robots have used a similar mechanism, incorporating additional actuators to modulate the angle of attack to actuate yaw. These include the 28 g Delfly Nimble [41, 21], the 19 g nano Hummingbird [44], and the 16.4 g KUBeetle-s [56].

Successful yaw actuation on minimally-actuated (one actuator per wing) have included a Robobee steered left and right using rapid, phased pitch and roll oscillations, exploiting the nonlinearity of attitude kinematics [30]. This expends significant energy, was hard to control, and was not able to consistently steer in a desired direction. In [27], a four-winged robot actuated yaw in free flight by extending the moment arm, but controlled flights in which yaw was controlled yaw were not demonstrated. More recently, a hummingbird-sized flapping-wing robot (12 grams) demonstrated control of all degrees of freedom, including yaw, using only two actuators [71].

Yaw torque in passively-pitching wings with a spring-like restoring moment was more closely investigated in [32]. That work revealed that due to the wing hinge and to the effect of taking the time-integral of drag force on the wing, the yaw torque could reverse sign. The magnitude of this "torque inversion" peaks at the peak lift-to-drag ratio. That work proposed additional features that established a nonlinear stress curve for the wing hinge, negating the torque inversion. Similarly, the two-actuator Purdue hummingbird uses a physical interlock to limit the range of wing pitch angle to avoid torque inversion [71].

Due to this challenge, no demonstration of yaw control on a minimal (two-actuator) vehicle with spring-like hinges has been made. It is not known whether wings with a physical limit to the angle of attack are more efficient than spring-like hinges, but the latter are likely to be quieter and may avoid fatigue-based failure. Steinmeyer et al. [64] showed that yaw

can be actuated successfully on a tethered flapper equipped with simple linear spring hinges if the robot is driven below its resonant frequency. At lower frequencies, the torque inversion regime can be avoided. But no controlled flight demonstrations have been reported to date. For controlled flight, cross-coupling between modes of actuation can either be neglected or modelled, both of which have associated challenges. In particular, the weaker the yaw actuation authority, the stronger the signal must be to attain consistent control over that degree of freedom. Anecdotal evidence suggests that the complicated motions of flapping-wing flight have cross-coupled interactions, which are exacerbated as the actuation signal increases. But in free-flight, a yaw controller must not disrupt other actuation modes. We conjecture that the foregoing challenges have precluded free-flight yaw control until now.

To address the problems mentioned in earlier research on yaw control, we introduce and validate two key innovations that are designed to increase yaw authority on vehicles with spring-like passive wing hinges. First, we show that a new robot fly design, that reorients its piezo actuators laterally and moves its wings farther from the center of mass to increase moment arm, is able to increase its yaw actuation authority. Called Robofly-Expanded (Fig 3.1) [22], we demonstrate that through this change it is able to actuate and control its yaw angle while hovering using PD control. The robot is able to follow simple trajectories while hovering. Second, we show that by changing the phase of the higher frequency excitation of the wings, even greater yaw torque is possible. We validate these results using quasi-steady analytical model for the flapping wing, as well as a lumped-parameter model of the actuator-wing system.

3.3 Yaw Torque Generation

3.3.1 Robot Design

As introduced in [22], the robot has its actuators re-oriented so that their long axes are horizontal and along the body pitch axis (Fig. 3.1). One of the desirable effects of moving the wings father apart from the center of mass (CM) of the body is a larger moment arm.

Table 3.1: Parameters and their values used for in simulations

Parameter	Symbol	Value
Density of air	ρ	1.23 $kg\ m^{-3}$
Distance from CM to CP	r_{cp}	2.03 cm
Distance from wing base to midpoint of the wing along its length	r_{b-w}	9.0 mm
Peak-to-peak wing amplitude	Φ	54°
Flapping frequency	$\frac{\omega}{2\pi}$	190 Hz
Wing hinge parameter	β	10.32 $ms^{-1}rad^{-1/2}$
Wing mass	m	0.63 mg
Stiffness of combined actuator and transmission	K_{act}	105 $\mu Nmrad^{-1}$
Vertical distance from wing center of pressure to hinge	z_{cp}	1.25 mm
Hinge stiffness	k	4.4 $\mu Nmrad^{-1}$
Wing area	A	51.2×10^{-6} m^2

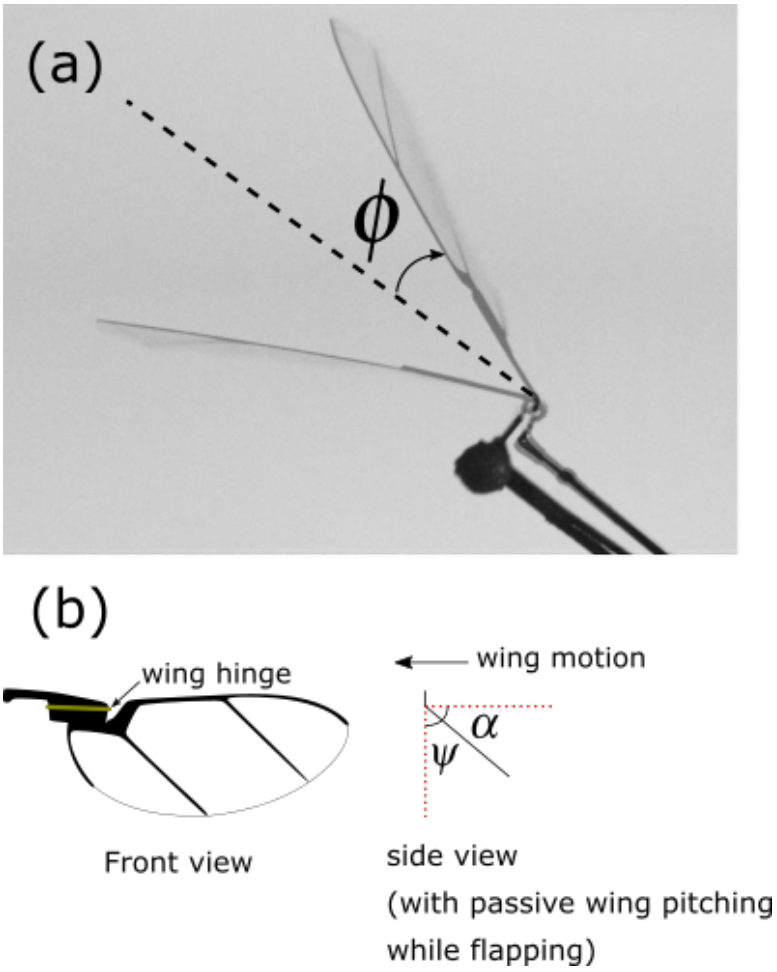

Figure 3.2: (a) Wing angle $\phi(t)$, measured using frames from high-speed video. The wing is flapped at 190 Hz, providing ≈10 frames per stroke. (b) A drawing of a wing in frontal view; its passive wing hinge can be seen. On the right is a side view (along the length of the wing) showing the passive wing pitching angle while flapping. The angle of attack, α, is measured relative to the horizontal plane, whereas wing hinge angle, ψ, is measured relative to the vertical plane.

The larger moment arm, coupled with drag induced by the flapping wings, leads to larger yaw torque generation.

The robot is also equipped with wider actuators which, in combination with the transmission, leads to a higher resonant flapping frequency of $\approx$ 200 Hz. Its wing hinges are passive spring-like flexure joints made of thin Kapton that produce passive pitching while flapping. They are 3$\times$ stiffer than those of Robofly [19] and Robobee [38] to match the 3$\times$ wider actuators. The effect of passive wing rotation is studied in detail and related equations of motion are derived in [24, 73]. The new design of actuators along with stiffer wing hinges allows the robot to lift more payload. For better yaw control authority, these robots are always flown with a lower payload than the maximum it can lift. This allows the robot to operate at off-optimal conditions, in which it produces significantly lower (yet larger than its own weight) lift than it can. The effect of the off-optimal conditions is explained in detail in the following subsection.

3.3.2 Torque generation

The only actuation mode that has produced measurable yaw torques consists of creating differential drag on wings by flapping them faster in one direction than the other. One of the ways to generate such split-cycle modulation is by actuating with voltage signal which also includes the second-harmonic frequency [49]. When the actuators are supplied with this voltage signal, the wing flapping angle, $\phi(t)$ is written as follows.

$$\phi(t) = \frac{\Phi}{2} \frac{\sin(\omega t) + \mu \sin(2\omega t)}{max[\sin(\omega t) + \mu \sin(2\omega t)]} \tag{3.1}$$

Here, ω is the wing angular velocity in rad/s, Φ is the peak-to-peak wing amplitude, and μ is the peak-to-peak amplitude of the second harmonic term, relative to the fundamental frequency term. The term μ is referred to as the second harmonic factor in the rest of the paper. The variation of wing angle while flapping is shown in Fig. 3.3 for $\mu = 0$ and for its extreme values of $+0.3$ and -0.3. We carried out experiments and observed that the total amplitude was the same for any value of μ, provided other parameters were kept constant.

Therefore, we used the normalizing term in Eq. 3.1 to match the peak-to-peak amplitude for any value of μ in the simulation.

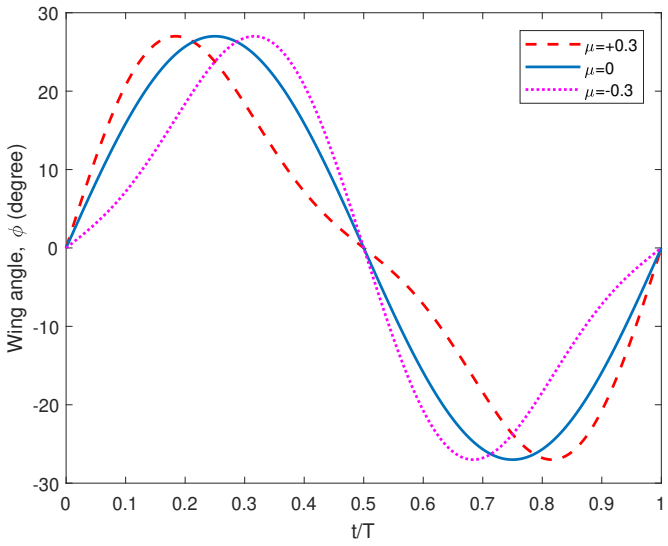

Figure 3.3: Wing angle $\phi(t)$, normalized by flapping time period, for three different values of the second harmonic factor μ. The wing angle ϕ is scaled so that the peak magnitude achieved in a given cycle is the same regardless of μ value.

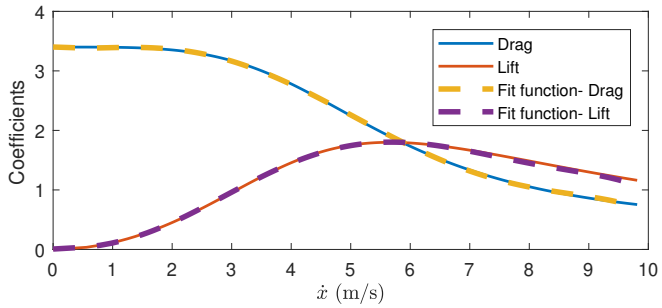

Figure 3.4: Model for C_{drag} and C_{lift} vs wing velocity $\dot{x}$ (translational velocity of the midpoint of the wing along its length) for Robofly wing hinge. Dashed lines indicate polynomial approximation used in simulation.

We present a model, inspired by [32], that entails purely-translational wing motion and a quasi-steady aerodynamic model to predict yaw torque behavior. The quasi-steady model

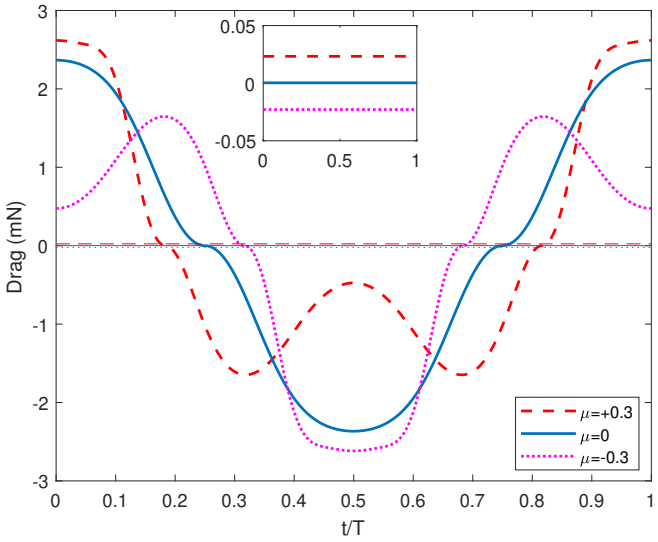

Figure 3.5: Simulation results of drag acting on a flapping wing changing with time (normalized by flapping time period), for three different values of μ. Non-zero values of μ show differential-drag generation. Horizontal lines on the main plot (also magnified in the inset) show the stroke-averaged drag values for corresponding values of μ.

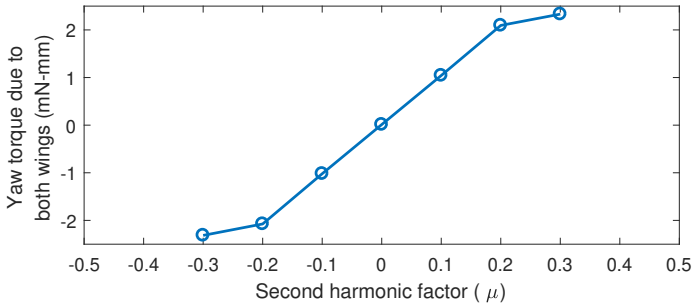

Figure 3.6: The variation of stroke-averaged yaw torque generated due to both wings with varying μ, according to the quasi-steady simulation.

incorporates unsteady flow effects in flapping wings such as the leading edge vortex into effective lift and drag coefficients [59, 60]. To simplify the simulation, we assume that wing rotation about its passive hinge is a direct function of wing flapping velocity, assuming that inertial dynamics around the wing hinge are fast relative to flapping frequency.

Drag acting on the wing, F_{drag}, is given by

$$F_{drag} = \frac{1}{2}\rho C_{drag}(\alpha) A r_{b-w}^2 \dot{\phi} \mid \dot{\phi} \mid \tag{3.2}$$

where A is wing area and ρ is air density. The quantity r_{b-w} is the distance from the wing base to the midpoint of the wing along its length, C_{drag} is the drag coefficient, which varies as a function of angle of attack (AoA) α [24, 73, 59] given by

$$C_{drag}(\alpha) = 1.9 - 1.5\cos(2\alpha) \tag{3.3}$$

Similarly, the lift force, F_{lift} is given by

$$F_{lift} = \frac{1}{2}\rho C_{lift}(\alpha) A r_{b-w}^2 \dot{\phi}^2, \tag{3.4}$$

where C_{lift} is the lift coefficient, a function of α [24, 73, 59], which is given by

$$C_{lift}(\alpha) = 1.8\sin(2\alpha). \tag{3.5}$$

C_{drag} and C_{lift} are functions of α. For simplicity, we model the system as a linearly translating wing, with position $x = r_{b-w}\phi$, where r_{b-w} is the distance to the midpoint of the wing along its length. If the α-axis dynamics are assumed to be instantaneous, then steady-state wing velocity is a function of α [32]:

$$\dot{x}_{ss} = \beta\sqrt{\frac{(\pi/2-\alpha)}{\sin(\pi/2-\alpha)C_{lift}(\alpha) + \cos(\pi/2-\alpha)C_{drag}(\alpha)}}, \tag{3.6}$$

where β is the wing hinge parameter [32] given by $\sqrt{\frac{2k_0}{\rho A z_{cp}}}$.

We performed a simple system identification procedure to determine the value of β. For this purpose, we flapped a wing with a bias signal of 250 V, a sinusoidal signal with a peak-to-peak amplitude $2V_0$ of 140 V to the middle layer (carbon fiber), and at 200 Hz. The

wing amplitude, ϕ, and AoA, α, were measured by recording the flapping of the wing using a high-speed camera (Phantom v7.3, Vision Research, Inc.) at 3900 frames per second. Frames at extreme positions of the flapping were captured to measure the peak-to-peak amplitude Φ. Fig. 3.2 shows an overlay of two frames in which the wing is at the extreme positions while flapping. With the measured amplitude, the wing angle was generated as a sinusoidal function of time. Wing velocity as a function of time was then calculated by taking the time derivative of the wing angle. This function was used to estimate the wing velocity, $\dot{x}_{ss}$ at mid-stroke ($\phi \approx 0$). We also estimated the corresponding α value by measuring the length of the projection of the wing chord in the overhead view. By substituting the values of $\dot{x}_{ss}$ and α in Eq. 3.6, we determined the value of β, which is specific to the Robofly wing hinge (Table 3.1).

We then substituted the value of β in Eq. 3.6 and plotted the steady state velocity as a function of α, for a possible range of velocities. We combined the steady-state velocity as the function of α with Eq. 3.3 and Eq. 3.5 and determined C_{lift} and C_{drag} as functions of the stead-state velocity. For this simulation we didn't consider the wing inertia and assumed $\dot{x} = \dot{x}_{ss}$. This assumption is consistent with the simplified translational quasi-steady model presented in [32]. We plotted the coefficients as the functions of $\dot{x}_{ss}$ in Fig. 3.4 along with the polynomial fit functions generated using Curve Fitting Toolbox in MATLAB.

Now, we move on to the simulation part which makes use of the empirical value of the wing hinge parameter. In this part, we decided to simulate for the flapping frequency of 190 Hz to slow down the dynamics in the corresponding experiments which are presented later. Using Eq. 3.4 and $C_{lift}(\dot{x})$, the required peak-to-peak wing amplitude (Φ) was determined such that the total lift was equal to the weight of the robot.

Referring to the wing angle plotted in Fig. 3.3 for three different values of μ, the drag was calculated using Eq. 3.2 for one whole cycle and plotted against time in Fig. 3.5. For $\mu = 0$, it can be seen that the drag force is symmetric about mean stroke position. However, in case of $\mu = 0.3$, the drag is significantly larger in one direction that the other. Similar but opposite pattern was observed in case of $\mu = -0.3$, as expected. The torque due to two

wings was then calculated using $\tau_{yaw} = 2r_{cp}F_{drag}$, where r_{cp} is the distance between the CM of the robot and the CP of the wing, projected on horizontal plane. τ_{yaw} is plotted for various values of μ in Fig. 3.6. The torque values estimated from the simulation are comparable with those from the simulation and experiments presented in [32]. It should also be noted that the torque estimated in our study was during a hovering flight (simulated) while holding a constant altitude i.e. the lift was also sufficient to support the weight of the robot.

Although our robot is able to generate a large amount of yaw torque as well as lift in the simulation and confirms no anomaly at the operating conditions, it is important to back the results using experiments. The analytical model presented in the work is simple translational quasi-steady, and it doesn't consider wing inertia in the wing pitching dynamics. Our model considers C_{drag} and C_{lift} as functions of wing velocity, and therefore it is more accurate than the models with constant drag and lift coefficients. However, it must be noted that these coefficients are calculated at every step considering that the wing velocity is under the steady state, ignoring the wing inertia. Additionally, actuator dynamics are also not considered in the model. However, we believe that the attenuation of the second harmonic frequency observed by [64] due to actuator dynamics can be addressed by increasing the amplitude of the second harmonic frequency beyond $0.3V_0$. A detailed modeling of a similar robot design can be referred to in [32, 64]. To address the limitations of the model in the paper and to ensure that enough amount of yaw torque is generated along with the required lift, demonstrations in hovering experiments are important.

3.4 Yaw Controller

We explained the hovering controller of the robot in detail in our earlier work on Robofly [18]. We combined the new yaw controller to work in parallel with the existing hovering controller (shown in Fig. A.1). The robot receives three inputs from the user, which include 1) altitude trajectory, 2) lateral position trajectory, and 3) heading trajectory.

The altitude trajectory is fed into the altitude controller which sends out thrust signals to the robot. The thrust is varied by changing the amplitude of sinusoidal signals supplied

to actuators. The lateral controller which is cascaded with the attitude controller receives the lateral trajectory as the input. The combination of the lateral and attitude controllers determines the roll and pitch torques given to the robot. The yaw controller developed in the current study is then added in parallel with these controllers.

The yaw controller receives the heading trajectory as the input and determines the second harmonic factor, μ', for sinusoidal signals that are supplied to actuators. The voltage signal supplied to the actuator is $V = V_0 [\sin(\omega t) + \mu' \sin(2\omega t)]$. All of these controllers receive feedback from a motion capture (MoCap) system (four Prime 13 cameras, OptiTrak, Inc., Salem, OR) for robot positions and orientations. This MoCap system sends the data over Ethernet at 240 Hz to the host computer running Simulink Real-Time. The data is sent further over to a xPC Target PC which runs the controller.

The heading, $\theta_d(t)$, is measured between global X-axis and robot's body x-axis (Fig. 3.1) and about global Z-axis. The feedback to the controller is the actual heading position, $\theta(t)$. The error, $e_\theta(t) = \theta_d(t) - \theta(t)$ is fed into a PD controller. The gains of the PD controller are hand-tuned to achieve the best performance. The control law is given by–

$$\mu' = k_{p\theta}\ e_\theta(t) + k_{d\theta}\ \dot{e}_\theta(t) \tag{3.7}$$

where $k_{p\theta}$ and $k_{d\theta}$ are the proportional and derivative gains, respectively. θ values received from MoCap are first filtered using a low-pass Butterworth filter (cutoff frequency of 240 Hz) before taking derivatives. The output yaw commands are bounded between -0.3 to $+0.3$.

3.5 Experiments

In this section we demonstrate three sets of results in which the robot follows a desired heading trajectory. In the first experiment, the desired set-point for the heading was held constant, while starting from a random initial heading. In the second experiment, we demonstrated the ability of the robot to steer in both directions. A set-point which changes quickly with time in both directions was given to the robot controller. In the third experiment, we demonstrated the ability of the robot to follow a heading trajectory. All of these experiments

were performed on a hovering robot. The flights were recorded using a high-speed camera from the location shown in Fig. 3.7.

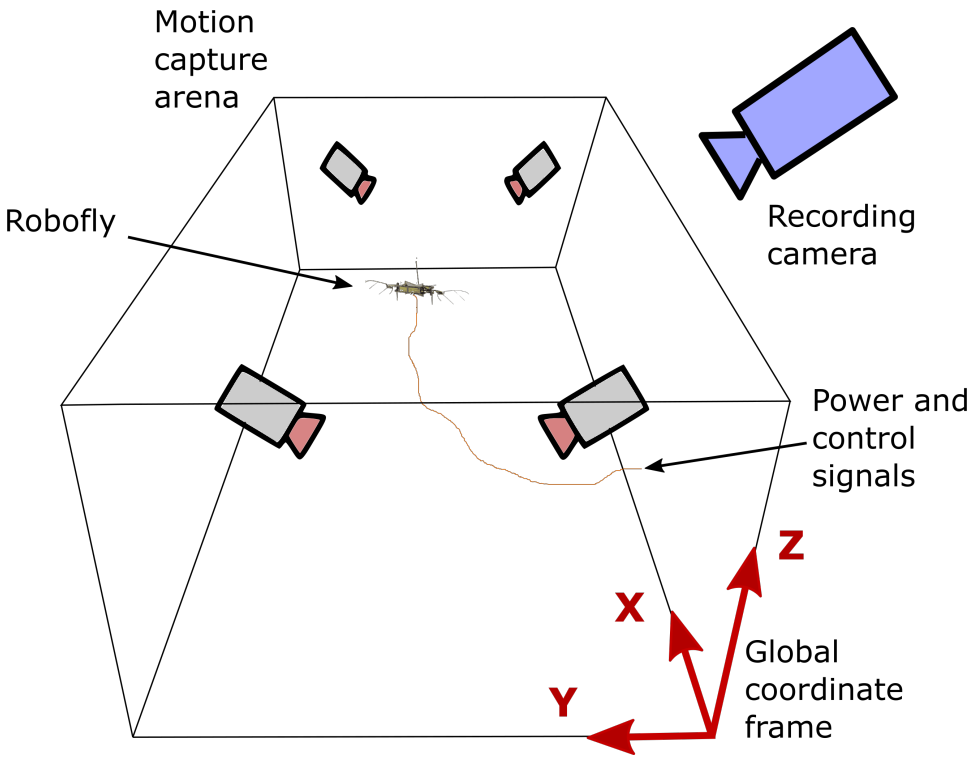

Figure 3.7: Motion capture arena. Global coordinate frame is shown for reference. Position of recording camera is shown for better understanding of the view in supplementary video and its frames. The absolute yaw angle (heading) of the robot is measured between body x axis and global X axis, about global Z-axis.

3.5.1 Constant set-point

Fig. 3.8 (top) represents the heading trajectory from two different flight experiments. The robot started from random values of initial headings. The first flight showed little overshoot and faster settling time; however, larger overshoot and longer settling time were observed in the second flight. This can be attributed to disturbances, including the wire tether and wind.

The robot approached and stayed at the set-point in both the flights after steady-states were achieved. The RMS errors for the last 0.7 sec in flight-1 and flight-2 are 4.46° and 6.47°, respectively. Yaw commands provided by the controller to actuators for the second flight are plotted in Fig. 3.8 (bottom). Frames from the second flight are shown in Fig. 3.9. Front of the robot is shown with an arrow in the first frame, and it can be observed in subsequent frames that the robot heading was at 0°.

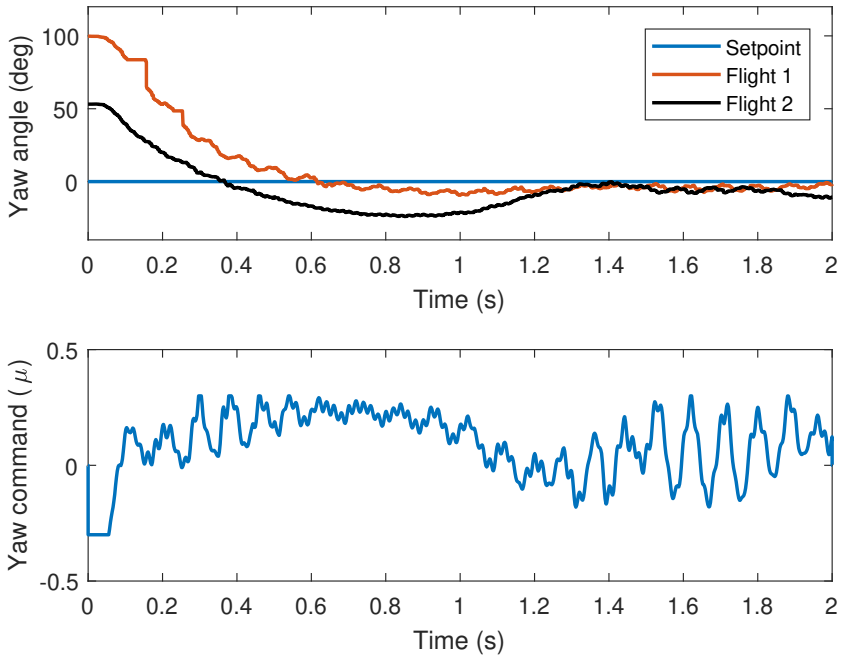

Figure 3.8: (Top) Step response of the yaw angle for two independent flights with different initial heading. The robot approaches the setpoint with a very small steady state error. (Bottom) Yaw command corresponding to flight-2 shows a strong control authority as the commands stays within the upper and lower bounds of $+0.3$ and -0.3, respectively.

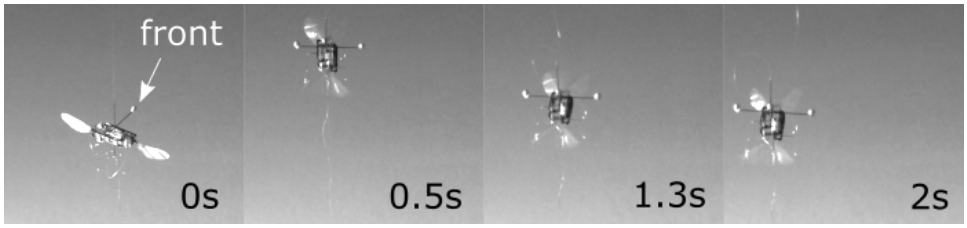

Figure 3.9: Frames from a video in which the robot approaches and maintains a constant heading of 0, which corresponds to a vector along the X-axis of the global coordinate frame.

3.5.2 Control authority in both directions

Although flight-2 in Fig. 3.8 (top) showed the ability of the robot to go back to the set-point after an overshoot, we carried out more experiments to demonstrate the control authority in both directions and the ability to react quickly to sharp changes in set-points in any direction. In this experiment, the robot followed a set-point that changed quickly (time period of 1 second) between $+60^\circ$ and 0°. Fig. 3.10 (top) shows the yaw angle response along with the given set-point in one of the flights demonstrating control authority in both directions.

3.5.3 Trajectory following

In Fig. 3.10 (bottom) it can be seen that the robot heading approached the desired set-point of $+60^\circ$ for first one second of the flight and zero heading for the next one second of the flight. During the flight, the robot could be seen steadying around the desired set-point before given the next set-point. The RMS error for the second set-point, calculated for last 0.5 sec is 0.33 rad. Frames from this flight are shown in Fig. 3.11. In the first frame, the robot heading before the take-off can be seen at $\sim 120^\circ$. In the middle frame, which was captured at 0.7s, the robot heading was controlled to be at around 60°. In the last frame, the robot was controlled to hover with zero heading.

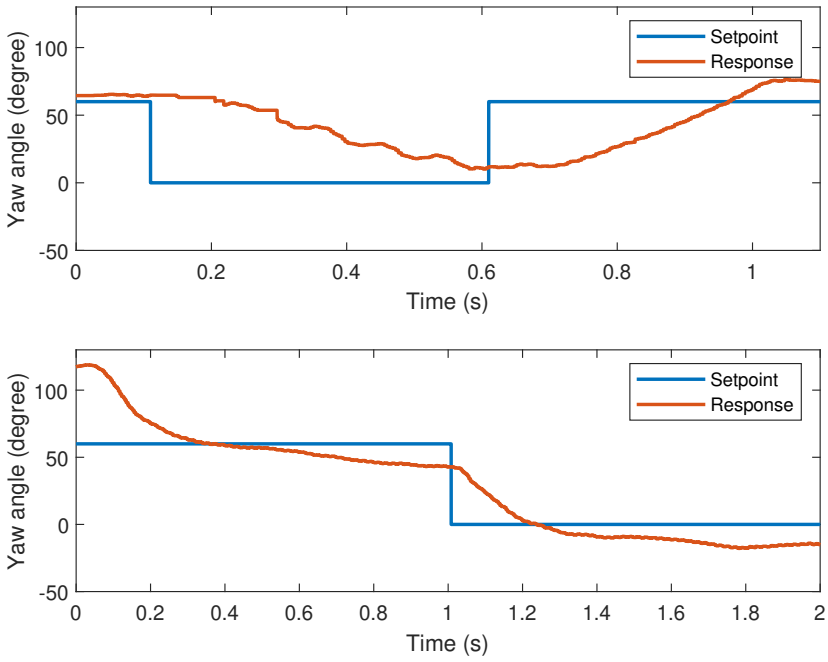

Figure 3.10: (Top) Yaw angle (degree) response in a flight in which the set-point is changed mid-flight to demonstrate control authority in both directions. (Bottom) Yaw angle (degree) response in a flight in which the set-point is changed mid-flight. The robot reacts quickly to the change in the set-point while hovering and approaches the set-point with small steady state error.

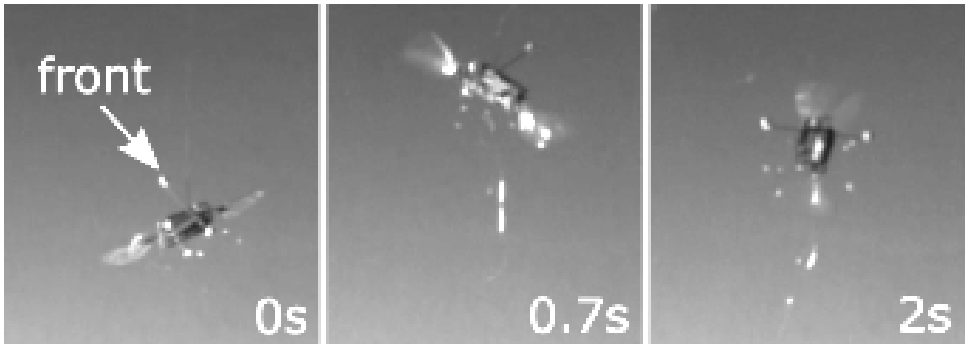

Figure 3.11: Frames from a video in which the robot approaches and follows a trajectory of heading. Intermittent frame shows the heading close to the set-point of 60°, and the final frame shows the heading close to 0. These angles are measured about the Z-axis of the global coordinate frame.

3.6 Further Increasing Yaw Torque by Adjusting Phase of The Second Harmonic

We have identified an additional mechanism by which to improve yaw torque. The basic principle is to compensate for any phase shift in the second harmonic as it passes through the wing-actuator drive system. If the system is driven slightly below the peak lift to drag ratio [64] to insure that there is no torque inversion [32], our results indicate that torque can be improved by adjusting the phase of the second harmonic frequency. The behavior of the actuator-transmission-wing system is well approximated by a second-order simple harmonic oscillator [26]. Frequencies higher than the resonant mode, such as the second harmonic, are strongly attenuated [64]. Of particular relevance in the current section is the observation that high frequencies are *also* delayed in phase, which, to our knowledge, has not previously been explored in detail. We note at the outset that phase plays an important role in yaw torque. A phase shift of 180° can reverse its direction, as shown in Fig. 3.12 (left). From the combined signal it can be seen that the wing would flap harder in one direction than the other. However, when a phase delay of 180° is introduced in the second harmonic signal (see Fig. 3.12 right), the opposite effect is observed. If the downstroke is faster than the upstroke

in the first case, the second would lead to the upstroke being faster than the downstroke, in the absence of any phase difference in the system response. Now, assuming we supply the combined signal shown in Fig. 3.12 (left) to the actuator, and the actuator-wing system introduces a phase difference between its response to the fundamental frequency and the second harmonic frequency, this can lead to a reduced yaw effect and, in some cases, torque in the opposite direction.

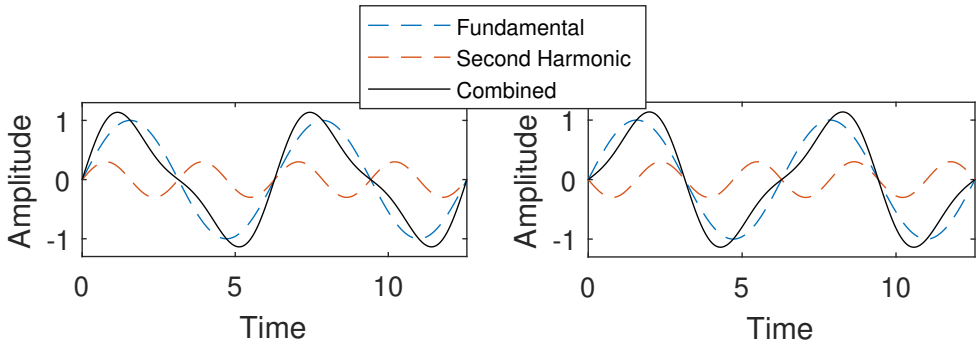

Figure 3.12: Sample drive signals given to the actuators for commanding yaw. The combined signal is the sum of the fundamental harmonic and second harmonic signals.

To understand how varying phase plays out in practice subject to the filtering effect of the resonant system, we created a simulation and tested the idea on a physical robot. The simulation combined the aerodynamics of linear translation of a wing on a passive hinge (Equations (3.2–3.6)) with a second-order lumped-parameter model of the dynamics of the actuator-wing system. The state of the simulation evolves according to

$$\dot{\psi} = \lambda(F_{\perp}(\psi, \dot{x})z_{cp} - k\psi) \tag{3.8}$$

$$\ddot{x} = \frac{1}{m}(F_{act} - k_{act}x + F_{drag}(\psi, \dot{x})) \tag{3.9}$$

where $F_{\perp} = F_{lift}\sin\psi + F_{drag}\cos\psi$ is perpendicular component of the aerodynamic total force acting on the wing and F_{act} is the force by the piezoelectric actuator acting on the translating wing, $k_{act} = K_{act}/r_{b-w}^2$ is the effective spring-like restoring stiffness of the system

as seen at the point r_{b-w} away from the stroke rotation axis, and m is the mass of the wing. The value λ must take on a large value to drive the dynamics of ψ to quickly satisfy Eq. 3.6 as $\dot{x}$ changes. It was chosen so that the bandwidth of the ψ dynamics ($=\lambda k$) is 3000 Hz.

This system was simulated using fixed-step numerical integration to estimate resulting x trajectories under conditions of zero and non-zero second harmonic contributions, driven by the function $F_{act} = f_0(\sin(\omega t) + \mu' \sin(2\omega t + \Theta))$, where ω is slightly below the resonant frequency, but still near optimal efficiency (Fig. 3.13). Fig. 3.14 shows that by adding positive phase to the second harmonic signal, yaw torque can be increased dramatically, by 36%.

To experimentally validate these results, we suspended the physical robot with a thin Kevlar thread and supplied a drive voltage with smaller amplitude than what is required for lift-off, while varying phase and second harmonic magnitude. The thin thread allowed the robot to spin freely about its yaw axis. We used the MoCap system to measure the maximum yaw velocity achieved after wing flapping started, which is an approximate and convenient way to measure relative yaw torque. The voltage signal supplied to the actuator, which is approximately proportional to actuator force, was $V = V_0 \left[\sin(\omega t) + \mu' \sin(2\omega t + \Theta)\right]$. Fig. 3.15 shows the resulting yaw velocities at steady-state. Note that the robot was not calibrated to have zero initial yaw torque; instead we show normalized yaw effect relative to that at $\mu' = 0$. The robot shows a stronger yaw torque at non-zero values of Θ, increasing with positive, which is consistent with the predictions of the simulation (Fig. 3.14). Similarly, a harmonic oscillator driven by a second harmonic above the resonant frequency would show phase lag; addition of phase lead would recover the ideal waveform shown in Fig. 3.3.

3.7 Conclusion

We have proposed and demonstrated experimentally three innovations by which to increase the yaw (z-axis) torque on flapping wing vehicles with a passive spring-like wing hinge. Our interest in such hinges is driven by their potential to be quieter less prone to failure than hinges with physical hinge angle limits [71]. The innovations are 1) a new robot fly design that increases the distance between the center of mass of the robot and the center of pressure of the

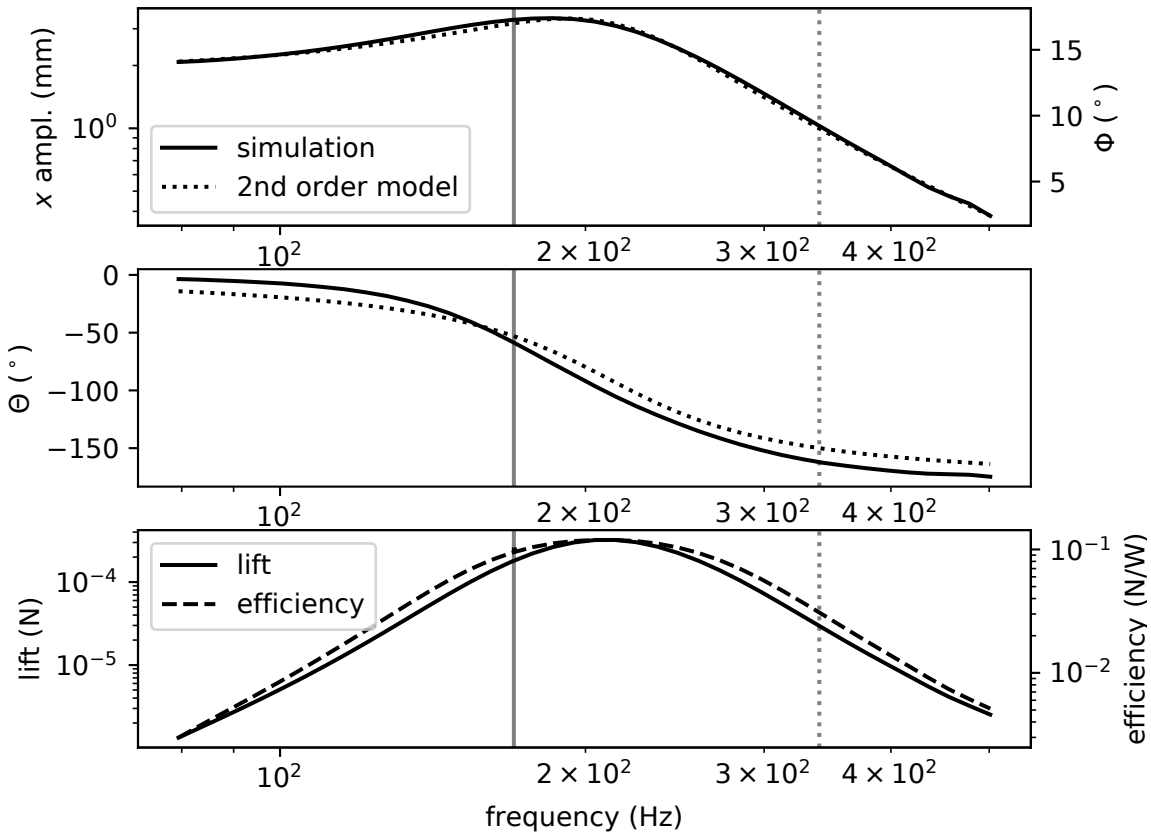

Figure 3.13: The frequency response of the simulated system (Eq. (3.9) resembles a second-order simple harmonic oscillator. (bottom row) The system was driven at 170 Hz (grey vertical line), near its peak efficiency and thrust; the second harmonic frequency is shown as a dashed line. The second harmonic is attenuated (causing $\mu << \mu'$) and has a phase lag. Efficiency $= \int F_{lift} dt / \int |F_{act} \dot{x}| dt$ over a complete cycle.

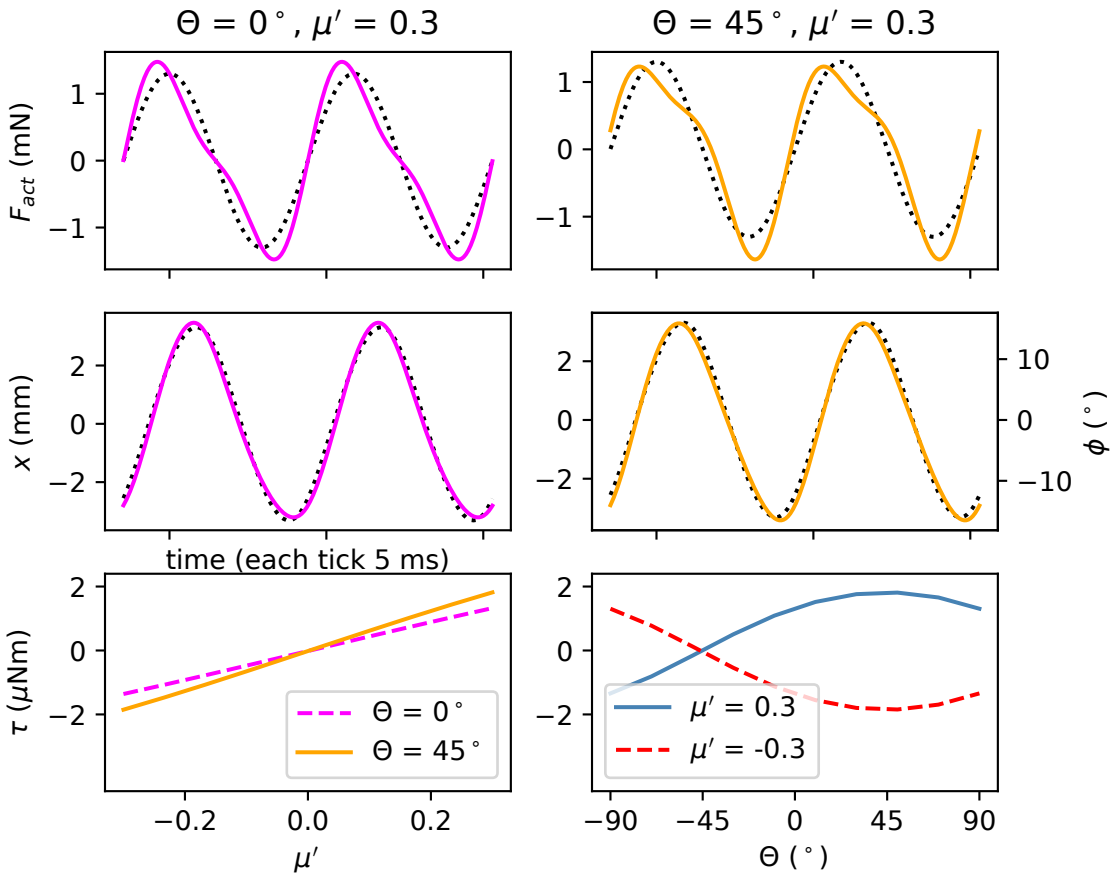

Figure 3.14: Simulation indicates that stronger torque can be produced by a second harmonic with a phase lead. (top row) Input actuator forces acting on the translating wing model at 170 Hz. Baseline signal (dotted) vs. with second harmonic (solid). On the left is no phase shift, the right shows a phase shift of 45°. (middle row) The output response of wing-actuator resonant system, which attenuates and phase-shifts the second harmonic signal. The right side shows that adding phase lead produces a more ideal wing motion with a faster upstroke and slower downstroke. (bottom row) Phase lead increases stroke-averaged yaw torque (compare to Fig. 3.15)

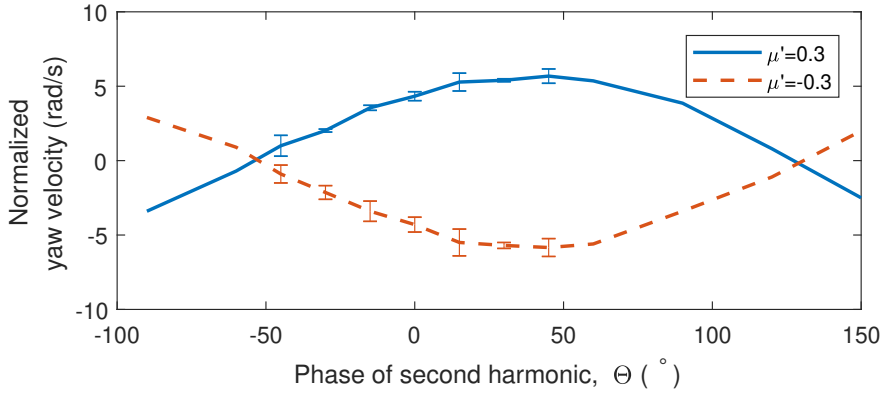

Figure 3.15: Experimental results show that adding phase lead Θ to the second harmonic can increase yaw torque, peaking at $\approx 45°$. In these experiments, the robot was hung by a thread and allowed to spin freely under the effect of a yaw command; data points show steady-state yaw velocity, minus the yaw velocity at $\mu' = 0$. Flapping frequency was 170 Hz, V_0=35. For values closer to $\Theta = 0$, three readings were taken, and the median was plotted along with error bar with length equal to the difference between the maximum and the minimum of the three values.

wings to increase the yaw torque moment arm, 2) wider actuators that increase the operating frequency, and 3) demonstration that the addition of a phase shift in the second harmonic signal can further increase yaw torque when driven off-resonance. We validated the results through simulation and robotic demonstration, showing for the first time, that it is possible to control yaw angle on such a vehicle while in controlled flight. This overcomes a significant limitation of previous two-actuator robot designs with spring wing hinges, which have been unable to actuate their yaw angle in controlled hovering flight [49, 19]. Experimental results were performed on a new design of an insect-sized aerial robot, called Robofly-expanded, weighing 160 mg. The robot design consists of two piezoelectric actuators and two wings to keep its design simple. Yaw torques were induced by adding a second harmonic signal to the fundamental frequency, resulting in differential drags in downstroke and upstroke. Our results build on [32] and [64], which revealed that the problem is more complicated than simply speeding up the upstroke relative to the downstroke.

The approach described here has the advantage of simplicity (two actuators vs. four) relative to the only other insect-sized system we are aware of that has achieved controlled yaw while hovering [67]. In the latter work, two additional piezoelectric actuators and a mechanism were incorporated to adjust the neutral angle of the wing hinge. Controlled yaw in controlled flight with a fully passive spring-like hinge has not previously been demonstrated, indicating the difficulty of the challenge. Actuation entails changes in wing kinematics that often affect other degrees of freedom, complicating flight control. A larger, 19 g hummingbird-sized robot has achieved a similar capability with only two actuators by using physical interlocks that limit the range of wing hinge angle [71].

Our results indicate that yaw torque is complex phenomenon and highly dependent on parameter values that are either hard to measure or prone to change. For example, wing inertia can change with the addition of a small amount of glue during repair. Circumstantial observations from our simulation suggest that when the system is driven at the resonant frequency, a phase shift does not improve yaw torque, which merits further investigation. Known effects of flapping-wing flight [58] were not incorporated into the present model for

simplicity, including viscosity, added mass, and the Kramer effect. Therefore, there may be additional mechanisms to actuate yaw that have not yet been explored. In practice, we propose that a phase tuning operation be added to the vehicle trimming process to maximize yaw torque [22].

Acknowledgements

Authors would like to thank Johannes James and Vikram Iyer for insightful discussion. Authors also appreciate Hari Krishna Hari Prasad's help during fabrication. This work was partially supported by the Air Force Office of Scientific Research under grant no. FA9550-14-1-0398.

Chapter 4

AUTONOMOUS ROBOFLY

Flying insect robots (FIR), inspired by biological insects like Drosophila, are inexpensive to manufacture, and have weight in the order of 200 mg. Hence, these robots' swarms have the potential to be used for applications like search and rescue operations, agricultural support, and space exploration. To enable such applications, the research to make these robots autonomous has been booming in the last decade.

As a step towards the autonomous flight, Robofly-Expanded with added capability, which includes onboard sensors for hovering, is discussed in this chapter. In previous demonstrations of controlled flight of similar MAVs [49, 27, 19], control relies on real-time feedback from a motion capture (MoCap) system consisting of four cameras, which track the robot as a rigid body moving in the cameras' frames. The robot's real-time position and orientation data are fed back into a dedicated PC running the controller as UDP packets over the ethernet, and a control signal is then generated and sent to the robot. As a result, the robot cannot show controlled behavior outside the MoCap arena due to the lack of real-time data.

To have the robot fly autonomously, onboard sensors must be capable of localizing the robot in its environment as well as sensing the robot's orientation. This work contributes lateral sensing using optical flow, which fits within the size, weight, and power (SWaP) constraints of the robot. A full set of sensors required for autonomy must additionally include altitude and orientation sensors.

Earlier research involved mounting sensors for attitude and altitude feedback for control. A gyroscope was included on an insect-sized robot for attitude stabilization as presented in [28]. Similarly, a bio-inspired vision sensor was included by [29] for flight control. [33] used an onboard magnetometer for pitch and yaw feedback. For altitude feedback, [34] used an

onboard time-of-flight sensor. However, these results were demonstrated on robot designs which carried only one sensor at a time. Also, the lateral motion sensing has not yet been addressed.

The rest of the chapter is organized as follows. First, the need for a new design of the robot is explained, followed by observability analysis to determine the number and types of sensors. Then, the sensors selection and integration are discussed in detail. The optical flow calculations are presented in detail in the following section. In the end, I conclude by presenting the experimental results and preliminary findings.

4.1 Robofly-Expanded

In order to achieve an autonomous flight, it is essential to have the sensors onboard for localization. The Robofly, presented in [19] and also in chapter 2, has a low payload capacity of ∼100 mg. Therefore, I decided to move to a heavier robot with larger payload capacity. This robot, Robofly-Expanded [22], also has a slightly different design with better yaw and pitch control. This robot design is the same as the one used for the yaw controller in chapter 3. The robot's payload is measured to be about 330 mg, which is sufficient for the MEMS sensors that are planned to be placed onboard this robot. A short-legged version of Robofly-Expanded is shown next to US penny in Fig. 4.1.

4.2 Observability Analysis

The dynamics of the system and the observability analysis for the state of the system are discussed in this section. For the robot to hover in space without drifting away laterally, it is vital to be able to estimate the lateral velocity. At the same time, it may not be easy to observe or measure the lateral position of the robot considering limited payload capacity of the robot. Therefore, leaving the lateral position out, the states of the system in two dimensional analysis are given by

$$q = \begin{bmatrix} \dot{x} & z & \dot{z} & \theta & \dot{\theta} \end{bmatrix}^T \tag{4.1}$$

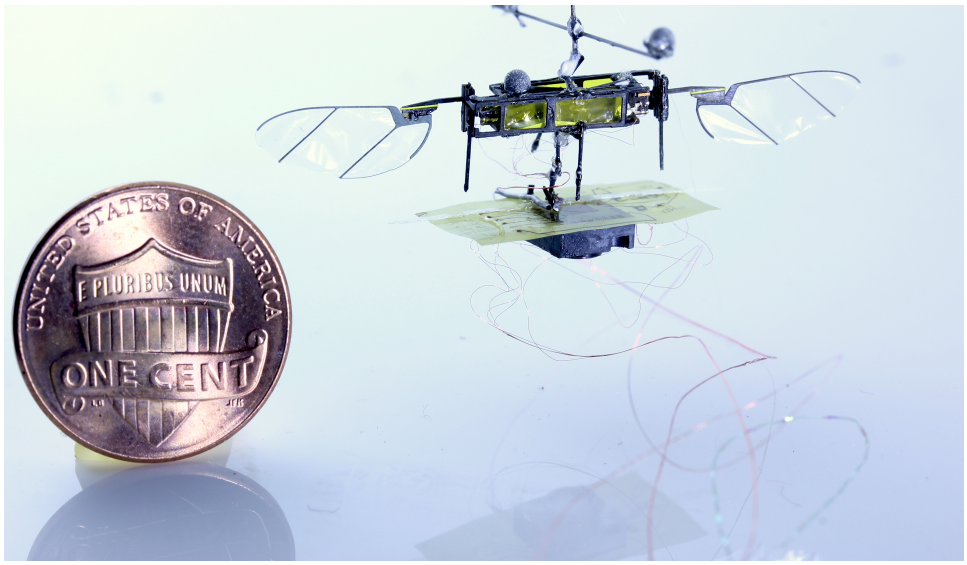

Figure 4.1: The Robofly-Expanded is an 335 mg (including sensor payload) flapping-wing robot capable of performing controlled flight using offboard sensors such as motion capture cameras. Here I implement the lateral motion control using an onboard optical flow sensor on this robot. A US penny is shown for scale.

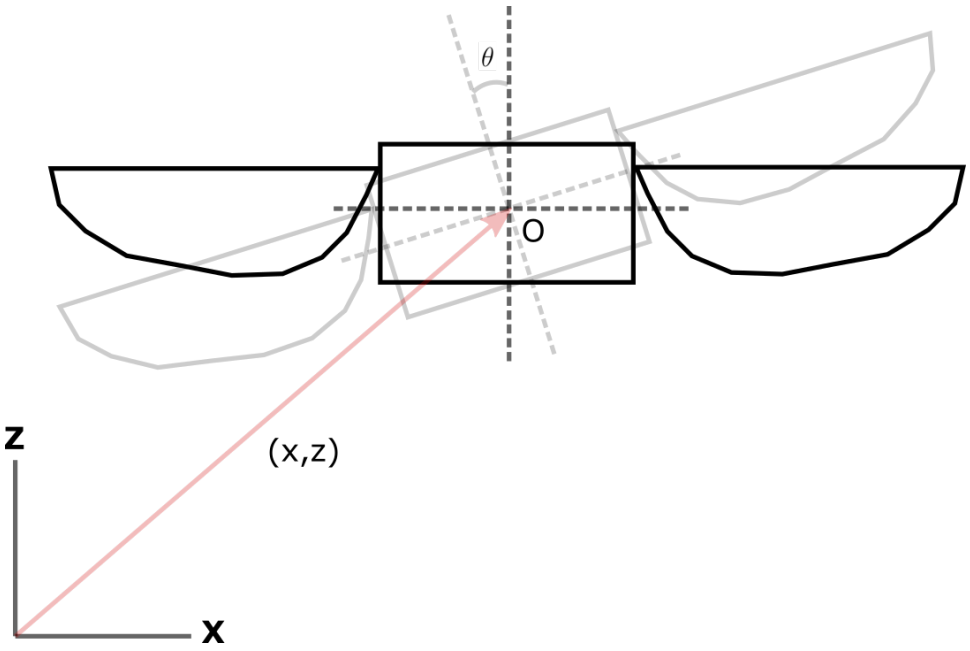

Figure 4.2: A two dimensional dynamic model of Robofly-Expanded

Here, x and z are the lateral and vertical positions in inertial coordinates system, respectively. θ and $\dot{\theta}$ are orientation and angular velocity of the body about Y-axis. The dynamic model of Robofly is shown in Fig. 4.2. In order to make the analysis simple, I start with the 2-dimensional analysis, which can be easily extended to 3-dimensional analysis as the three planes in which roll, pitch and yaw motions are observed, are considered to be decoupled.

The equations of motion of the system in x and z can be written as follows. These equations are after the linearization about a stable equilibrium state, $q_0 = \begin{bmatrix} 0 & z_d & 0 & 0 & 0 \end{bmatrix}^T$, and at thurst, $T = mg$.

$$\ddot{x} = g \sin\theta = g\theta \tag{4.2a}$$

$$\ddot{z} = \frac{T}{m} - g = 0 \tag{4.2b}$$

The state space representation of the dynamics of the system can be written as follows.

$$\dot{q} = Aq + Bu \tag{4.3a}$$

$$y = Cq \tag{4.3b}$$

Here A and B are defined as follows.

$$A = \begin{bmatrix} 0 & 0 & 0 & g & 0 \\ 0 & 0 & 1 & 0 & 0 \\ 0 & 0 & 0 & 0 & 0 \\ 0 & 0 & 0 & 0 & 1 \\ 0 & 0 & 0 & 0 & 0 \end{bmatrix}; \quad B = \begin{bmatrix} 0 \\ 0 \\ 0 \\ 0 \\ 0 \end{bmatrix}$$

However, C depends on the sensors and their measurements. As mentioned above, the ultimate goal is to include three sensors onboard– 1) a time of flight (ToF) for altitude z, 2) a gyroscope for angular velocities ω, and 3) an optical flow sensor for relative motion with respect to the ground. The sensor output and hence matrix C are given as in Eq. 4.4 and 4.5. The optical flow sensor output is linearized about a constant altitude, z_d.

$$y = \begin{bmatrix} \tilde{z} \\ \tilde{\omega} \\ \omega - \frac{\dot{x}}{z} \end{bmatrix} \tag{4.4}$$

$$C = \begin{bmatrix} 0 & 1 & 0 & 0 & 0 \\ 0 & 0 & 0 & 0 & 1 \\ -\frac{1}{z_d} & 0 & 0 & 0 & 1 \end{bmatrix} \tag{4.5}$$

Once the dynamics of the system is determined, the next task is to find out if all the states for designing the controller can be observed. MATLAB was used to find out that the pair (A, C) is observable.

Figure 4.3: Robofly-Expanded is shown next to an optical flow sensor.

4.3 Sensor Selection and Integration

As per the observability analysis presented above, the Robofly needs at least three sensors to hover autonomously. I considered IR ToF sensor for altitude, mainly because of its success with RoboBee as presented in [34]. For sensing attitude, I turned to a gyroscope for its simplicity and proven success [28]. Other sensors considered were ocelli inspired photodiodes [29]. I don't intend to use an accelerometer or a magnetometer for this study. Now, for the lateral sensing, I had an option of using a set of ToF sensors in lateral directions; however, considering the limitations on computation and the payload capacity, I turned to an optical flow sensor, which can estimate lateral velocities when its data is fused with that of the attitude and altitude sensors. An optical flow sensor next to the robot is shown in Fig. 4.3

In the first part of the autonomous flight of Robofly, the objective is to use the optical flow

sensor onboard which corresponds to the third row in matrix C, and other two rows of the data in matrix C are simulated using data from the motion capture system (MoCap) (Model Prime13, OptiTrack, Inc., Salem, OR) in real-time. The MoCap sends data at 240 Hz over the ethernet to the host computer which runs MATLAB real-time, which further sends the data to the target PC as UDP packets. Through a Simulink block the altitude and angular velocities measurements are simulated as actual sensors data by adding some noise and bias to the real-time data.

4.3.1 Sensors

Though it is important to have the lateral motion sensor working first, the ultimate goal is a fully autonomous insect-sized robot. In this chapter, a large emphasis is given to the lateral motion control with onboard sensor. I list down the sensors, that are explored and that can eventually go onboard for control autonomy.

The ToF sensor used for altitude sensing is ST VL53L1X which has a range of up to 4 m and frequency up to 50 Hz. Average power consumption at room temperature is reported to be 20 mW [6]. The potential gyroscope that can be used for this study is Bosch BMG250. It is a low noise, low power (current $\sim 850\mu A$) three axial gyroscope [3].

As the first step in lateral motion sensing, I consider an object motion sensing chip, PMW3901MB-TXQT (Pixart Imaging, Inc., Hsinchu, Taiwan) and lens assembly LN03-ZSZ. The working range of the sensor is 80 mm to infinity [5]. The sensor with the lens assembly weighs 115 mg. As mentioned above, it measures the optical flow due to the relative motion between the robot and the ground surface. Robot's lateral velocities with respect to the ground are then calculated by fusing the sensor data with ω and Z_d data from MoCap. The sensor has proven to be successful for lateral motion sensing in larger drones [4].

4.3.2 Sensor Circuit

The optical flow sensor was assembled in a flight-weight package weighing 132 mg as seen in Fig. 4.4. A sensor breakout circuit was designed and etched on Dupont Pyralux AC

091200EV flexible circuit material. Any required discrete components such as resistors, capacitors, and WLCSP voltage regulator were selected in smallest commercially available packages to minimize weight.

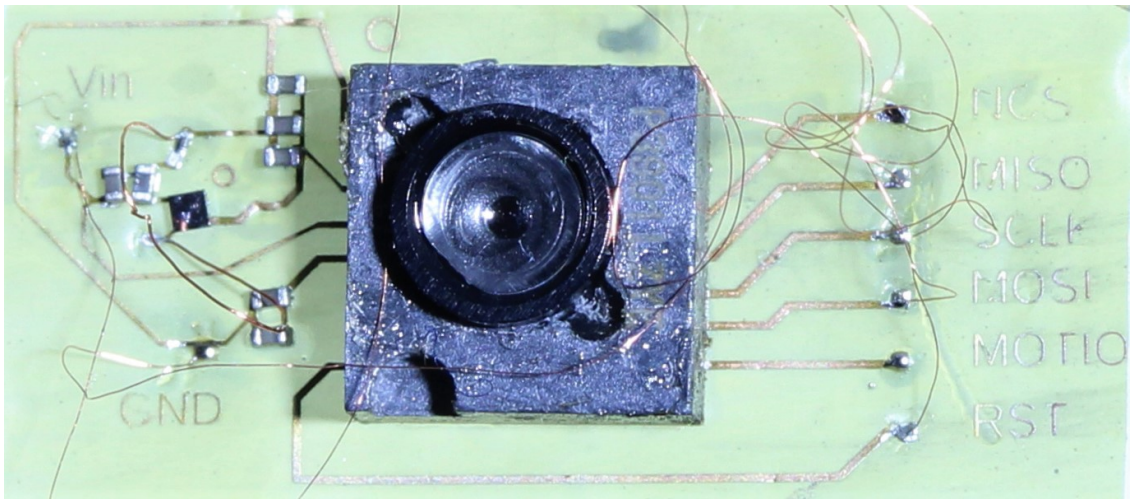

Figure 4.4: 132 mg optical flow sensor circuit implementation

4.3.3 Sensor Communication

The optical flow sensor which is facing downward was mounted onboard the robot. This sensor, through its circuit, communicates with a microcontroller (Arduino Uno) board over SPI communication. An RS-232 shield was installed on the Arduino board, which was used for communication with the xPC (Target PC) over a RS-232 cable. The data communication happens at about 100 Hz with a 37 ms of delay. The sensor communication path is shown in Fig. 4.5.

4.3.4 Calibration

The optical flow sensor was calibrated first by comparing its estimates with corresponding MoCap measurements as the ground truth. It was performed by attaching four retro-

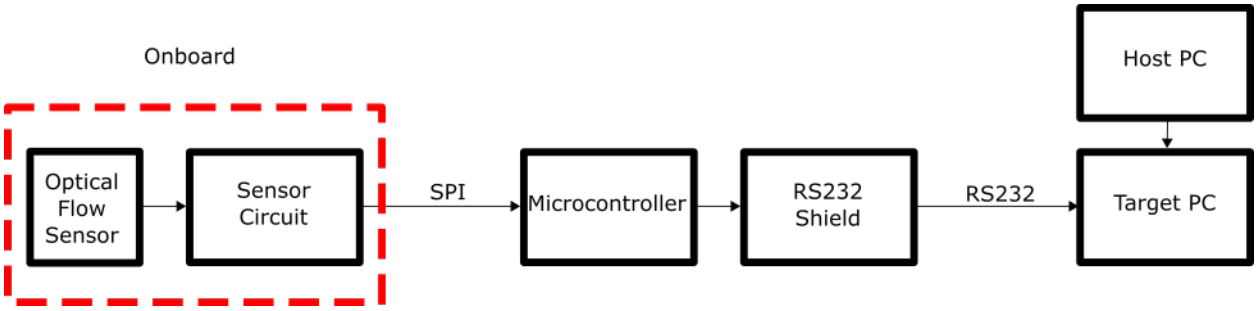

Figure 4.5: A block diagram of sensor communication. The optical flow sensor, through its circuit, communicates with a microcontroller offboard, which accepts SPI communication and further communicates with the controller PC (xPC Target PC) through RS232 communication.

reflective markers on a wand with the sensor facing downwards and by moving it manually inside the MoCap arena. The altitude was kept constant for the calibration experiment, and the wand was moved in the horizontal plane. It was made sure that the rigid body was free from any angular motion. One of the possible setups tried out for calibration is shown in Fig. 4.6. The comparison of optical flow sensor's lateral velocity estimates with the corresponding values from MoCap system is shown in Fig. 4.7 and Fig. 4.8.

4.3.5 Sensor Placement Scheme

As the output of optical flow sensor is linearized about a constant altitude, z_d, it is important to place the sensor on the robot where the variation in the altitude is minimal. Therefore, I placed it underneath the center of mass of the robot, as seen in Fig. 4.1. The setup apparatus is also drawn in Fig. 4.9.

4.4 Optical Flow

Optical flow is the measurement of the relative motion between the camera sensor and the object in front of it. It is calculated from the change in the intensity of pixels between two

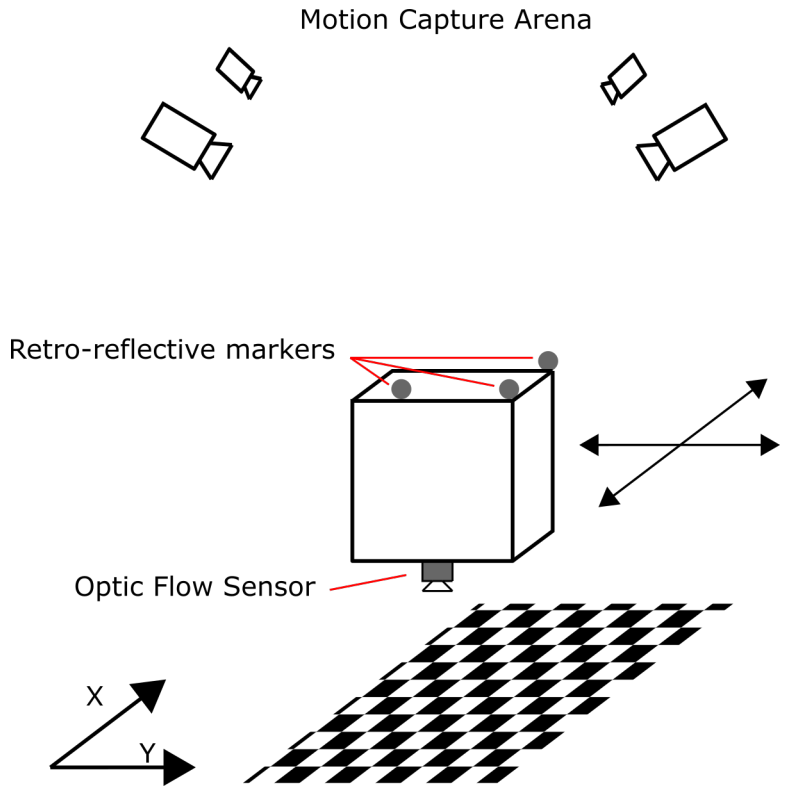

Figure 4.6: Calibration setup for the optical flow sensor. The sensor is mounted on a rigid body with retro-reflective markers on it. These markers are tracked by the motion capture system, which serves as the ground truth for the position and orientation data.

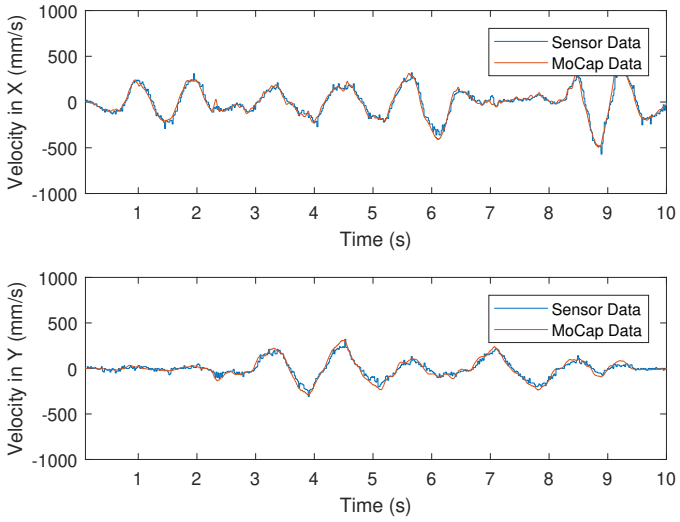

Figure 4.7: Sensor data (unfiltered) and MoCap data plotted on top of each other with respect to time

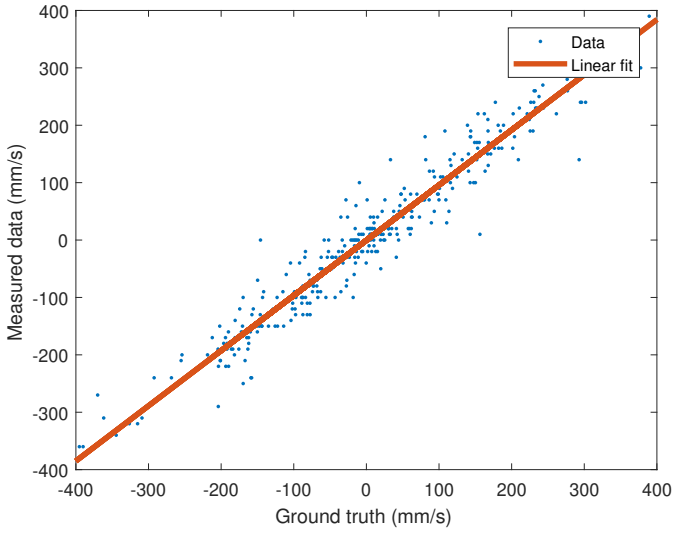

Figure 4.8: Comparison of sensor measurements with MoCap measurements (ground truth). A best fit line computed was: $\hat{z} = 0.96z - 0.44$, where $\hat{z}$ is the sensor measurement and z is the corresponding ground truth

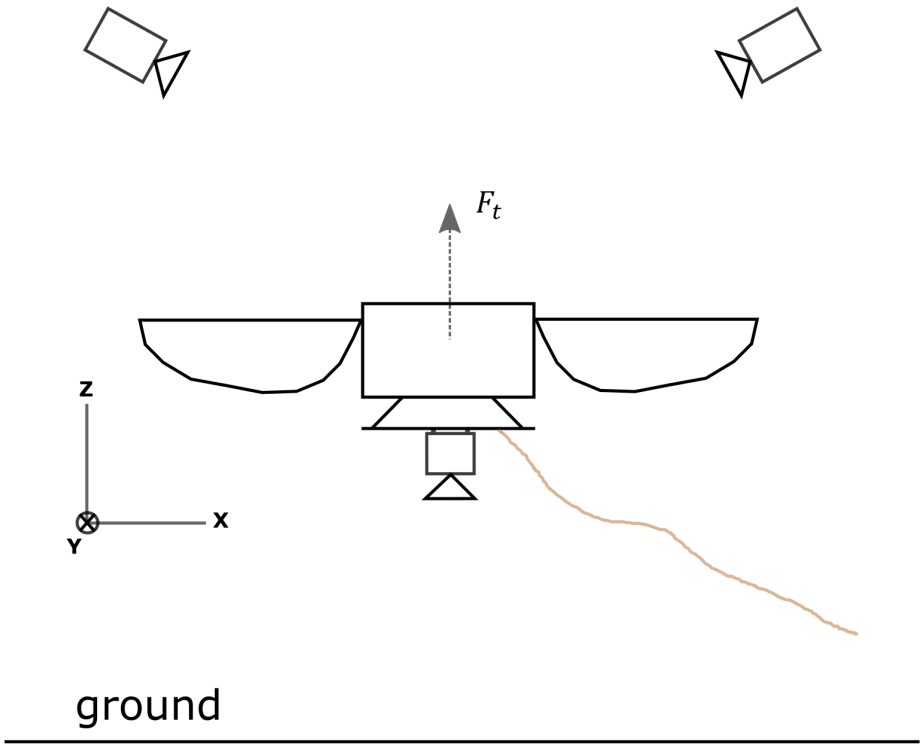

Figure 4.9: Model of the Robofly-Expanded with the apparatus for flight. The lateral controller assumes the control of attitude and altitude, which are sensed using motion capture system. This reduces the system to two dimensions which are the lateral position (X and Y). The optical flow sensor mounted below the robot, combined with the MoCap data, estimates the lateral velocities of the robot. A set of 51-gauge copper tethers is used for power, control as well as sensor communications.

consecutive frames in time. Since the optical flow is the relative motion between the camera sensor and the object, it is a combination of both translational and rotational motion of the sensor as well as the object. In our case the sensor is mounted facing downwards on the robot, whereas the object is the ground. Since the ground is assumed to be stationary, optical flow is nothing but a combination of robot's translational and rotational motion.

For convenience and simplicity of the calculation, the camera (local) coordinate system is aligned with the global coordinate system when the robot is stationary and the camera is facing downwards.

OF_x and OF_y are the optical flow estimations from the camera sensor along local x and y axes, respectively. f is the focal length of the lens, which is experimentally found out to be 10 cm for PMW3901 sensor lens. $\hat{V}_x$ and $\hat{V}_y$ are the lateral velocity estimations from the optical flow sensor. These velocities are measured in the global coordinate systems. ω_x and ω_y are the velocities of the sensor about global X and Y axes, respectively. Then the optical flow estimation by the sensor, in the simplest case of no yaw motion ω_z, is given by Eq. 4.6.

$$\begin{bmatrix} \mathrm{OF}_x \\ \mathrm{OF}_y \end{bmatrix} = \frac{1}{z} \begin{bmatrix} f & 0 \\ 0 & f \end{bmatrix} \begin{bmatrix} \hat{V}_x \\ \hat{V}_y \end{bmatrix} + \begin{bmatrix} 0 & -f \\ f & 0 \end{bmatrix} \begin{bmatrix} \omega_x \\ \omega_y \end{bmatrix} \tag{4.6}$$

Once the optical flow estimates are determined from the sensor, the data is fused with the angular velocity estimates, ω_x and ω_y, and altitude, z, from the MoCap.

4.5 Experiments

4.5.1 Hovering flight with MoCap data, without using the data from the onboard sensor

The first step in the experiments starts with performing trimming in open-loop flights. For this purpose, the robot was suspended using a Kevlar thread which exerts negligible torque on the robot as compared to other payload. The robot was flown for a short duration (0.3 s), and the flight was recorded using a high frame-rate camera. Trimming was performed by manually observing and correcting torques with the help of the slow-motion videos of the flights. This process of open-loop flying is repeated until the robot takes off vertically upright.

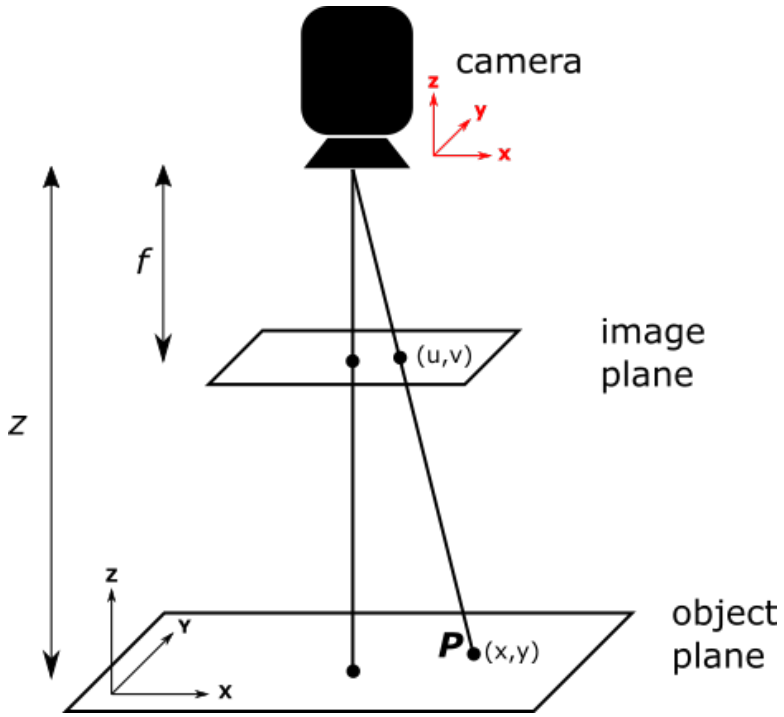

Figure 4.10: The relation between the optical flow data and the relative motion between the camera and the object plane. Detailed calculations are presented in [15].

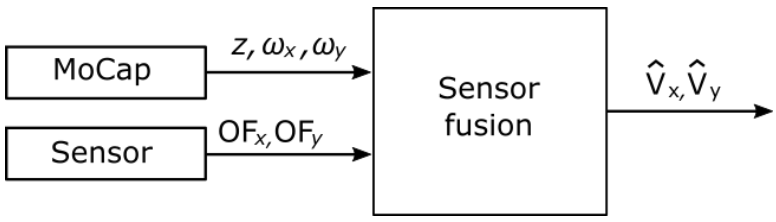

Figure 4.11: The sensor fusion, required for lateral velocity estimates, involves MoCap and optical flow sensor data

Once the trimming was done, the next step was to perform closed-loop flights. The controller used in closed-loop flights is explained in detail in [18]. In the closed-loop experiments, the robot was flown with the lateral motion estimates from MoCap system to determine controller gains.

In the hovering flights, I used the MoCap estimates for all attitude, altitude, and lateral motion controller. By carrying out these flights, I observed that the robot was able to fly with the onboard optical flow sensor, and the onboard sensor values closely matched the estimates from the MoCap system, which were treated as the ground truth. The images from the hovering flight are shown in Fig. 4.12.

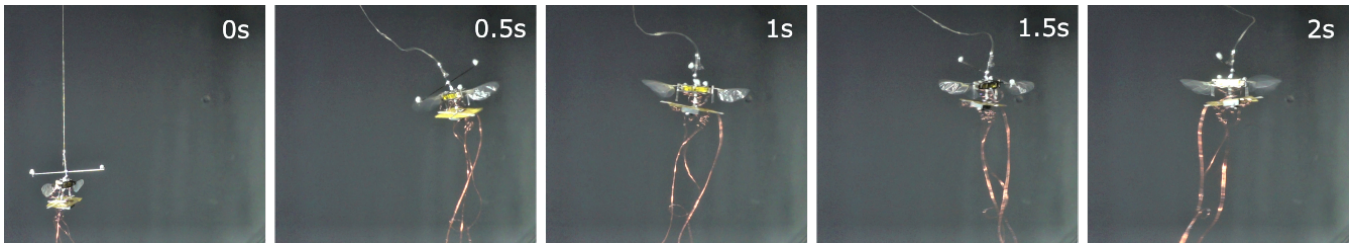

Figure 4.12: Snapshots of hovering Robofly-Expanded mounted with optical flow sensor. The robot is controlled by an altitude and a lateral controller running in parallel.

4.5.2 Sensor in the loop

Once the angular velocity and altitude data were fused with sensor optical flow estimates in real-time, the next objective was to use the lateral velocity estimates to control the robot position in the horizontal plane while hovering. The same controller was used for this closed-loop study; however, the sensor estimates instead of MoCap data were fed into the lateral controller. The lateral velocity estimates were integrated in time to get the lateral position. The trajectory from a hovering flight is given in Fig. 4.13. The roll and pitch tilts, as commanded by the lateral controller, which used the sensor data for lateral position, are shown in Fig. 4.14. These tilts were also compared with the tilts that the lateral controller

using MoCap estimates for the position would command.

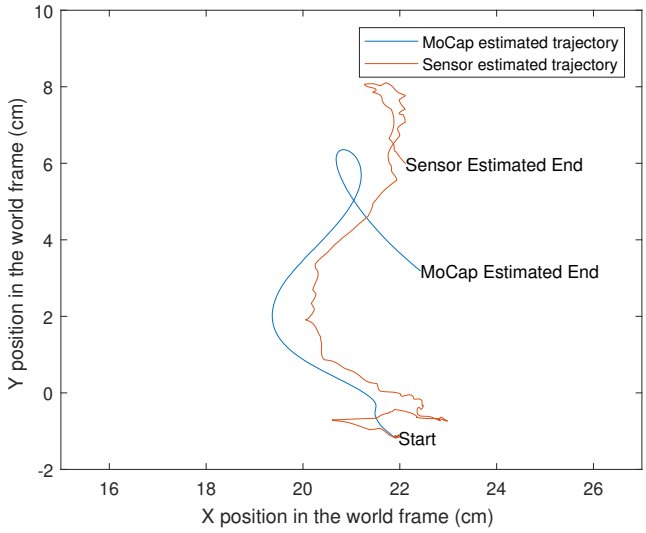

Figure 4.13: 2D trajectory of a flight with lateral position feedback from onboard optical flow sensor

4.6 Conclusion

Hovering flights of insect-sized robots are not yet fully controlled without real-time data from offboard sensors such as Motion Capture (MoCap) system. In this chapter, I explored options of onboard sensors for a fully autonomous flight. There have been flights at this scale with only one sensor at a time and which only included a gyroscope for attitude control [28] and a time-of-flight IR sensor for altitude control [34]. The lateral motion of the robots was yet to be controlled using an onboard sensor. In this chapter, I focused on an optical flow sensor for the lateral motion control. I miniaturized the sensor package and mounted it on the robot. I also briefly discussed the communication of this sensor with the controller PC. I presented calibration results that compared lateral velocity estimates from the onboard sensor data with that from the ground truth MoCap data. In the experimental results, I presented a short flight that used onboard sensor data for control. The lateral position

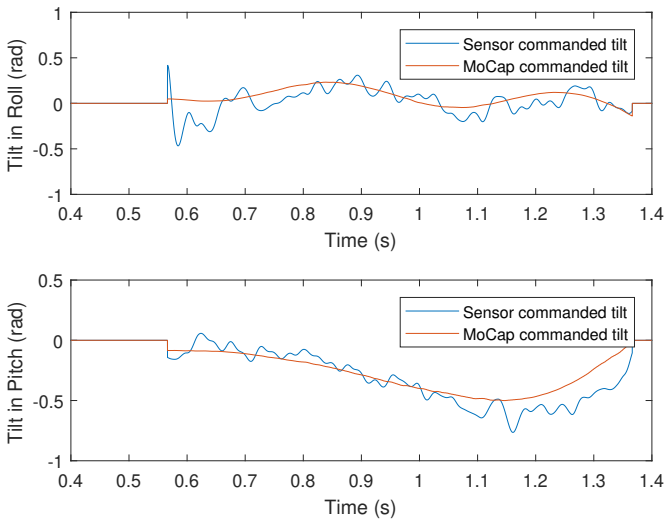

Figure 4.14: Comparison of commanded tilts from lateral controllers using MoCap and sensor estimates for position, in roll and pitch directions

estimates comparison with that from the MoCap (which was used only for tracking and not for controlling) shows a close match.

4.7 Future Work

Once the robot starts flying for longer using the optical flow sensor data for the feedback, the next step will be to use a Bluetooth chip onboard to get rid of wire tethers needed for sensor communication. The ultimate goal will be to include all the three sensors mentioned in this chapter, along with the Bluetooth chip for wireless communication, which will make the robot fully control-autonomous.

Acknowledgment

This work is partially supported by the Air Force Office of Scientific Research under grant no. FA9550-14-1-0398. I wish to thank Johannes James, Daksh Dhingra, and Vikram Iyer for insightful discussions and help during the study.

Chapter 5
CONCLUSIONS AND DISCUSSION

The work presented in this dissertation addresses various issues in mobility autonomy and control autonomy of insect-sized flapping-wing robots. The work ranges from a new design and a novel fabrication technique to controlling the robot while performing multimodal locomotion.

5.1 New Design: Robofly

Chapter 2 introduced a new design for insect-sized flapping-wings robots, the UW Robofly. The major contributions of the chapter include 1) simplified fabrication and assembly to reduce errors and misalignment, 2) the new design enables the robot to land in uncontrolled flights, 3) the ability to perform ground locomotion or walking in addition to flying to ensure operations in confined spaces with overhead obstacles, and 4) further modification to the robot gives it the ability to perform waterstriders-like locomotion on the water surface.

5.2 Yaw Angle Control Using Passive Wing Hinge

There have been insect-sized robots, including the one presented in chapter 2, capable of performing a controlled roll, pitch, and lateral motion. However, heading (absolute yaw angle) control was never achieved on these robots due to insufficient yaw torque generation while hovering. Controlling the heading is essential for capturing images or recording videos of surroundings with an onboard camera. Chapter 3 introduced a yaw controller for a new design of Robofly, Robofly-expanded. It generates yaw torque by flapping one stroke harder than the other and thus creating a net differential drag. The yaw controller on this robot was possible due to the larger distance between its center of mass and the center of pressure

of the wings. Also, the robot with wider actuators has the ability to lift-off with a larger payload and flap at a higher frequency; therefore, it can operate at off-optimal conditions while carrying little or no payload. First, we demonstrated using simulations the ability of the robot to generate sufficient torque while supporting its own weight through lift. We then demonstrated through experiments the ability of the robot to steer towards the desired setpoint of the heading while hovering. We also identified another way to optimize the yaw effect in simulation and experiments and laid down the foundation for future work.

5.3 Control Autonomy

Insect-sized robots to date cannot fly without real-time feedback from the offboard MoCap system. If these robots are to fly freely in nature, they need to be fully autonomous and rely on onboard sensors for feedback. In chapter 4, I proposed a sensor suite for Robofly within its payload capacity. I showed, using observability analysis, that the sensor suite can estimate the required states for the robot to fly autonomously. Researchers have used a gyroscope for attitude sensing and an IR sensor for altitude sensing in the past. In this research, we took a step further towards a fully autonomous flight by using an optical flow sensor onboard for sensing the lateral motion of the robot. We demonstrated through hovering experiments that the data from the optical flow sensor closely matches with ground truth. We also demonstrated a short flight that used the onboard sensor data for lateral motion feedback.

5.4 Future Directions

The field of insect-sized flapping robots draws inspiration from nature and is quite challenging because of the physics involved at the micro-scale. There have been some recent developments in the power autonomy of these robots; however, to get rid of all the tethers, making these robots control autonomous is essential. The future direction also involves including more onboard sensors that can preform operation-specific tasks such as gas leak detection and plant monitoring. However, this may further require roboticists to improve the payload capacity of these robots. It will also demand more energy out of the onboard power source.

Therefore, in order to use these robots for carrying out real world applications, roboticists need to consider the design, power autonomy, and control autonomy, all at once.

BIBLIOGRAPHY

[1] Autonomous Insect Robotics Laboratory, University of Washington. Available: `http://depts.washington.edu/airlab/RoboFly_hovering.html`. 2019.

[2] Autonomous Insect Robotics Laboratory, University of Washington. Available: `http://depts.washington.edu/airlab/IROS2018-1906.html`. 2018.

[3] Bosch BMG250 Datasheet. Accessed August 2020: https://www.bosch-sensortec.com/media/boschsensortec/downloads/datasheets/bst-bmg250-ds000.pdf.

[4] Crazyflie 2.0 Flow deck. Accessed August 2020: https://www.bitcraze.io/2017/07/crazyflie-2-0-flow-deck/.

[5] Pixart PMW3901MB. Accessed August 2020: https://www.pixart.com/products-detail/44/PMW3901MB-TXQT.

[6] VL53L1X Datasheet. Accessed August 2020: https://www.st.com/resource/en/datasheet/vl53l1x.pdf.

[7] R McNeill Alexander. *Principles of animal locomotion*. Princeton University Press, 2003.

[8] Richard J Bachmann, Frank J Boria, Ravi Vaidyanathan, Peter G Ifju, and Roger D Quinn. A biologically inspired micro-vehicle capable of aerial and terrestrial locomotion. *Mechanism and Machine Theory*, 44(3):513–526, 2009.

[9] Siuakumar Balasubramanian, Yogesh M Chukewad, Johannes M James, Geoffrey L Barrows, and Sawyer B Fuller. An insect-sized robot that uses a custom-built onboard camera and a neural network to classify and respond to visual input. In *2018 7th IEEE International Conference on Biomedical Robotics and Biomechatronics (Biorob)*, pages 1297–1302. IEEE, 2018.

[10] Palak Bhushan and Claire Tomlin. An insect-scale untethered laser-powered jumping microrobot. *arXiv preprint arXiv:1908.03282*, 2019.

[11] Matthew Bryant, Eric Wolff, and Ephrahim Garcia. Aeroelastic flutter energy harvester design: the sensitivity of the driving instability to system parameters. *Smart Materials and Structures*, 20(12):125017, 2011.

[12] John WM Bush and David L Hu. Walking on water: biolocomotion at the interface. *Annu. Rev. Fluid Mech.*, 38:339–369, 2006.

[13] Yufeng Chen, Neel Doshi, Benjamin Goldberg, Hongqiang Wang, and Robert J Wood. Controllable water surface to underwater transition through electrowetting in a hybrid terrestrial-aquatic microrobot. *Nature communications*, 9(1):2495, 2018.

[14] Yufeng Chen, Hongqiang Wang, E Farrell Helbling, Noah T Jafferis, Raphael Zufferey, Aaron Ong, Kevin Ma, Nicholas Gravish, Pakpong Chirarattananon, Mirko Kovac, et al. A biologically inspired, flapping-wing, hybrid aerial-aquatic microrobot. *Science Robotics*, 2(11):eaao5619, 2017.

[15] Pakpong Chirarattananon. A direct optic flow-based strategy for inverse flight altitude estimation with monocular vision and imu measurements. *Bioinspiration & biomimetics*, 13(3):036004, 2018.

[16] Pakpong Chirarattananon, Kevin Y Ma, and Robert J Wood. Adaptive control for take-off, hovering, and landing of a robotic fly. In *2013 IEEE/RSJ International Conference on Intelligent Robots and Systems*, pages 3808–3815. IEEE, 2013.

[17] Pakpong Chirarattananon and Robert J Wood. Identification of flight aerodynamics for flapping-wing microrobots. In *Robotics and Automation (ICRA), 2013 IEEE International Conference on*, pages 1389–1396. IEEE, 2013.

[18] Yogesh M Chukewad, Johannes James, Avinash Singh, and Sawyer Fuller. Robofly: An insect-sized robot with simplified fabrication that is capable of flight, ground, and water surface locomotion. *arXiv preprint arXiv:2001.02320*, 2020.

[19] Yogesh M Chukewad, Avinash T Singh, Johannes M James, and Sawyer B Fuller. A new robot fly design that is easier to fabricate and capable of flight and ground locomotion. In *2018 IEEE/RSJ International Conference on Intelligent Robots and Systems (IROS)*, pages 4875–4882. IEEE, 2018.

[20] Ludovic Daler, Stefano Mintchev, Cesare Stefanini, and Dario Floreano. A bioinspired multi-modal flying and walking robot. *Bioinspiration & biomimetics*, 10(1):016005, 2015.

[21] Guido CHE De Croon, MA Groen, Christophe De Wagter, Bart Remes, Rick Ruijsink, and Bas W van Oudheusden. Design, aerodynamics and autonomy of the delfly. *Bioinspiration & biomimetics*, 7(2):025003, 2012.

[22] Daksh Dhingra, Yogesh M Chukewad, and Sawyer B Fuller. A device for rapid, automated trimming of insect-sized flying robots. *IEEE Robotics and Automation Letters*, 5(2):1373–1380, 2020.

[23] Michael H Dickinson and Karl G Gotz. Unsteady aerodynamic performance of model wings at low reynolds numbers. *Journal of Experimental Biology*, 174(1):45–64, 1993.

[24] Michael H Dickinson, Fritz-Olaf Lehmann, and Sanjay P Sane. Wing rotation and the aerodynamic basis of insect flight. *Science*, 284(5422):1954–1960, 1999.

[25] Charles Porter Ellington. The aerodynamics of hovering insect flight. vi. lift and power requirements. *Phil. Trans. R. Soc. Lond. B*, 305(1122):145–181, 1984.

[26] Benjamin M Finio, Néstor O Pérez-Arancibia, and Robert J Wood. System identification and linear time-invariant modeling of an insect-sized flapping-wing micro air vehicle. In *2011 IEEE/RSJ International Conference on Intelligent Robots and Systems*, pages 1107–1114. IEEE, 2011.

[27] Sawyer B Fuller. Four wings: An insect-sized aerial robot with steering ability and payload capacity for autonomy. *IEEE Robotics and Automation Letters*, 4(2):570–577, 2019.

[28] Sawyer B Fuller, E Farrell Helbling, Pakpong Chirarattananon, and Robert J Wood. Using a mems gyroscope to stabilize the attitude of a fly-sized hovering robot. 2014.

[29] Sawyer B Fuller, Michael Karpelson, Andrea Censi, Kevin Y Ma, and Robert J Wood. Controlling free flight of a robotic fly using an onboard vision sensor inspired by insect ocelli. *Journal of The Royal Society Interface*, 11(97):20140281, 2014.

[30] Sawyer B Fuller, John P Whitney, and Robert J Wood. Rotating the heading angle of underactuated flapping-wing flyers by wriggle-steering. In *2015 IEEE/RSJ International Conference on Intelligent Robots and Systems (IROS)*, pages 1292–1299. IEEE, 2015.

[31] MA Graule, P Chirarattananon, SB Fuller, NT Jafferis, KY Ma, M Spenko, R Kornbluh, and RJ Wood. Perching and takeoff of a robotic insect on overhangs using switchable electrostatic adhesion. *Science*, 352(6288):978–982, 2016.

[32] Nick Gravish and Robert J Wood. Anomalous yaw torque generation from passively pitching wings. In *2016 IEEE International Conference on Robotics and Automation (ICRA)*, pages 3282–3287. IEEE, 2016.

[33] E Farrell Helbling, Sawyer B Fuller, and Robert J Wood. Pitch and yaw control of a robotic insect using an onboard magnetometer. In *2014 IEEE international conference on robotics and automation (ICRA)*, pages 5516–5522. IEEE, 2014.

[34] E Farrell Helbling, Sawyer B Fuller, and Robert J Wood. Altitude estimation and control of an insect-scale robot with an onboard proximity sensor. In *Robotics Research*, pages 57–69. Springer, 2018.

[35] David L Hu and John WM Bush. The hydrodynamics of water-walking arthropods. *Journal of Fluid Mechanics*, 644:5–33, 2010.

[36] David L Hu, Brian Chan, and John WM Bush. The hydrodynamics of water strider locomotion. *Nature*, 424(6949):663, 2003.

[37] Vikram Iyer, Elyas Bayati, Rajalakshmi Nandakumar, Arka Majumdar, and Shyamnath Gollakota. Charging a smartphone across a room using lasers. *Proceedings of the ACM on Interactive, Mobile, Wearable and Ubiquitous Technologies*, 1(4):143, 2018.

[38] Noah T Jafferis, Moritz A Graule, and Robert J Wood. Non-linear resonance modeling and system design improvements for underactuated flapping-wing vehicles. In *2016 IEEE International Conference on Robotics and Automation (ICRA)*, pages 3234–3241. IEEE, 2016.

[39] Noah T Jafferis, E Farrell Helbling, Michael Karpelson, and Robert J Wood. Untethered flight of an insect-sized flapping-wing microscale aerial vehicle. *Nature*, 570(7762):491–495, 2019.

[40] Johannes James, Vikram Iyer, Yogesh Chukewad, Shyamnath Gollakota, and Sawyer B Fuller. Liftoff of a 190 mg laser-powered aerial vehicle: The lightest wireless robot to fly. In *2018 IEEE International Conference on Robotics and Automation (ICRA)*, pages 1–8. IEEE, 2018.

[41] Matěj Karásek, Florian T Muijres, Christophe De Wagter, Bart DW Remes, and Guido CHE de Croon. A tailless aerial robotic flapper reveals that flies use torque coupling in rapid banked turns. *Science*, 361(6407):1089–1094, 2018.

[42] Michael Karpelson, Benjamin H Waters, Benjamin Goldberg, Brody Mahoney, Onur Ozcan, Andrew Baisch, Pierre-Marie Meyitang, Joshua R Smith, and Robert J Wood. A wirelessly powered, biologically inspired ambulatory microrobot. In *Robotics and Automation (ICRA), 2014 IEEE International Conference on*, pages 2384–2391. IEEE, 2014.

[43] Michael Karpelson, Gu-Yeon Wei, and Robert J Wood. Driving high voltage piezoelectric actuators in microrobotic applications. *Sensors and actuators A: Physical*, 176:78–89, 2012.

[44] Matthew Keennon, Karl Klingebiel, and Henry Won. Development of the nano hummingbird: A tailless flapping wing micro air vehicle. In *50th AIAA aerospace sciences meeting including the new horizons forum and aerospace exposition*, page 588, 2012.

[45] Zaeem A Khan and Sunil Kumar Agrawal. Design of flapping mechanisms based on transverse bending phenomena in insects. In *Robotics and Automation, 2006. ICRA 2006. Proceedings 2006 IEEE International Conference on*, pages 2323–2328. IEEE, 2006.

[46] Je-Sung Koh, Eunjin Yang, Gwang-Pil Jung, Sun-Pill Jung, Jae Hak Son, Sang-Im Lee, Piotr G Jablonski, Robert J Wood, Ho-Young Kim, and Kyu-Jin Cho. Jumping on water: Surface tension–dominated jumping of water striders and robotic insects. *Science*, 349(6247):517–521, 2015.

[47] Bokeon Kwak and Joonbum Bae. Locomotion of arthropods in aquatic environment and their applications in robotics. *Bioinspiration & biomimetics*, 13(4):041002, 2018.

[48] Fei Li, Weiting Liu, Xin Fu, Gabriella Bonsignori, Umberto Scarfogliero, Cesare Stefanini, and Paolo Dario. Jumping like an insect: Design and dynamic optimization of a jumping mini robot based on bio-mimetic inspiration. *Mechatronics*, 22(2):167–176, 2012.

[49] Kevin Y Ma, Pakpong Chirarattananon, Sawyer B Fuller, and Robert J Wood. Controlled flight of a biologically inspired, insect-scale robot. *Science*, 340(6132):603–607, 2013.

[50] Kevin Y Ma, Samuel M Felton, and Robert J Wood. Design, fabrication, and modeling of the split actuator microrobotic bee. In *Intelligent Robots and Systems (IROS), 2012 IEEE/RSJ International Conference on*, pages 1133–1140. IEEE, 2012.

[51] James H Marden and Michael A Thomas. Rowing locomotion by a stonefly that possesses the ancestral pterygote condition of co-occurring wings and abdominal gills. *Biological Journal of the Linnean Society*, 79(2):341–349, 2003.

[52] Haripriya Mukundarajan, Thibaut C Bardon, Dong Hyun Kim, and Manu Prakash. Surface tension dominates insect flight on fluid interfaces. *Journal of Experimental Biology*, 219(5):752–766, 2016.

[53] Yash Mulgaonkar, Brandon Araki, Je-sung Koh, Luis Guerrero-Bonilla, Daniel M Aukes, Anurag Makineni, Michael T Tolley, Daniela Rus, Robert J Wood, and Vijay Kumar. The flying monkey: a mesoscale robot that can run, fly, and grasp. In *Robotics and Automation (ICRA), 2016 IEEE International Conference on*, pages 4672–4679. IEEE, 2016.

[54] Thomas J Nugent and Jordin T Kare. Laser power beaming for defense and security applications. In *Unmanned systems technology XIII*, volume 8045, page 804514. International Society for Optics and Photonics, 2011.

[55] Kevin Peterson and Ronald S Fearing. Experimental dynamics of wing assisted running for a bipedal ornithopter. In *Intelligent Robots and Systems (IROS), 2011 IEEE/RSJ International Conference on*, pages 5080–5086. IEEE, 2011.

[56] Hoang Vu Phan, Steven Aurecianus, Taesam Kang, and Hoon Cheol Park. Kubeetles: An insect-like, tailless, hover-capable robot that can fly with a low-torque control mechanism. *International Journal of Micro Air Vehicles*, 11:1756829319861371, 2019.

[57] Chris Roh and Morteza Gharib. Honeybees use their wings for water surface locomotion. *Proceedings of the National Academy of Sciences*, 2019.

[58] Sanjay P Sane. The aerodynamics of insect flight. *Journal of experimental biology*, 206(23):4191–4208, 2003.

[59] Sanjay P Sane and Michael H Dickinson. The control of flight force by a flapping wing: lift and drag production. *Journal of experimental biology*, 204(15):2607–2626, 2001.

[60] Sanjay P. Sane and Michael H. Dickinson. The aerodynamic effects of wing rotation and a revised quasi-steady model of flapping flight. *The Journal of Experimental Biology*, 205:1087–1096, 2002.

[61] Yun Seong Song and Metin Sitti. Surface-tension-driven biologically inspired water strider robots: Theory and experiments. *IEEE Transactions on robotics*, 23(3):578–589, 2007.

[62] Pratheev S Sreetharan, John P Whitney, Mark D Strauss, and Robert J Wood. Monolithic fabrication of millimeter-scale machines. *Journal of Micromechanics and Microengineering*, 22(5):055027, 2012.

[63] Ryan St. Pierre and Sarah Bergbreiter. Toward autonomy in sub-gram terrestrial robots. *Annual Review of Control, Robotics, and Autonomous Systems*, 2:231–252, 2019.

[64] Rebecca Steinmeyer, P Hyun Nak-seung, E Farrell Helbling, and Robert J Wood. Yaw torque authority for a flapping-wing micro-aerial vehicle. In *2019 International Conference on Robotics and Automation (ICRA)*, pages 2481–2487. IEEE, 2019.

[65] Kit Sum Wu, Jerome Nowak, and Kenneth S Breuer. Scaling of the performance of insect-inspired passive-pitching flapping wings. *Journal of the Royal Society Interface*, 16(161):20190609, 2019.

[66] Vamsi Talla, Bryce Kellogg, Benjamin Ransford, Saman Naderiparizi, Shyamnath Gollakota, and Joshua R Smith. Powering the next billion devices with wi-fi. In *Proceedings of the 11th ACM Conference on Emerging Networking Experiments and Technologies*, page 4. ACM, 2015.

[67] Zhi Ern Teoh. *Design of hybrid passive and active mechanisms for control of insect-scale flapping-wing robots*. PhD thesis, 2015.

[68] Zhi Ern Teoh and Robert J Wood. A flapping-wing microrobot with a differential angle-of-attack mechanism. In *2013 IEEE International Conference on Robotics and Automation*, pages 1381–1388. IEEE, 2013.

[69] Zhi Ern Teoh and Robert J Wood. A bioinspired approach to torque control in an insect-sized flapping-wing robot. In *5th IEEE RAS/EMBS International Conference on Biomedical Robotics and Biomechatronics*, pages 911–917. IEEE, 2014.

[70] William SN Trimmer. Microrobots and micromechanical systems. *Sensors and actuators*, 19(3):267–287, 1989.

[71] Zhan Tu, Fan Fei, Jian Zhang, and Xinyan Deng. An at-scale tailless flapping-wing hummingbird robot. i. design, optimization, and experimental validation. *IEEE Transactions on Robotics*, 2020.

[72] John P Whitney, Pratheev S Sreetharan, Kevin Y Ma, and Robert J Wood. Pop-up book mems. *Journal of Micromechanics and Microengineering*, 21(11):115021, 2011.

[73] John P Whitney and Robert J Wood. Aeromechanics of passive rotation in flapping flight. *Journal of fluid mechanics*, 660:197–220, 2010.

[74] Robert J Wood. The first takeoff of a biologically inspired at-scale robotic insect. *IEEE transactions on robotics*, 24(2):341–347, 2008.

[75] Robert J Wood, Ben Finio, Michael Karpelson, Kevin Ma, Néstor Osvaldo Pérez-Arancibia, Pratheev S Sreetharan, Hiro Tanaka, and John Peter Whitney. Progress on 'pico'air vehicles. *The International Journal of Robotics Research*, 31(11):1292–1302, 2012.

[76] Sui Zhou, Weiping Zhang, Yang Zou, Xijun Ke, Feng Cui, and Wu Liu. Piezoelectric driven insect-inspired robot with flapping wings capable of skating on the water. *Electronics Letters*, 53(9):579–580, 2017.

Appendix A

ADDITIONAL FIGURES

Fig. A.1 shows the block diagram of the hovering controller used in this research. It can be seen that the yaw controller works in parallel with lateral and altitude controllers explained in Fig. 2.10

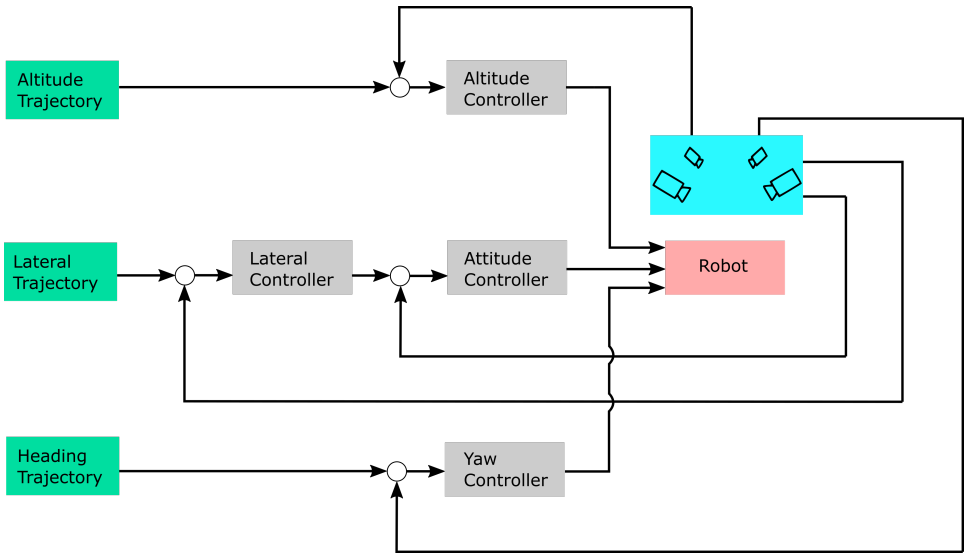

Figure A.1: Block diagram of the entire hovering controller of Robofly used for hovering while controlling the heading